

Master's Programme in mechanical engineering

The fracture toughness of elastic-brittle two-dimensional hierarchical square lattice

Akseli Leraillez

Author Akseli Leraillez

Title of thesis The fracture toughness of elastic-brittle two-dimensional hierarchical square lattice

Programme Master's programme in mechanical engineering

Major Solid mechanics

Thesis supervisor Assistant Professor Luc St-Pierre

Thesis advisor(s) Doctoral Candidate Milad Omid

Date 15.07.2022	Number of pages 75	Language English
------------------------	---------------------------	-------------------------

Abstract

Lattice materials are often used in applications that require material properties not offered by solid materials. The wide range of material properties offered by lattice materials are especially useful in application that require lightweight and strong materials. Strong and lightweight materials are needed to build larger structures and reduce transportation costs. The material properties of regular lattices are well known, but hierarchical lattices have not been extensively studied. Especially the fracture toughness of hierarchical lattices is not well known even though fracture toughness is important for practical applications as cracking is a common problem.

This thesis aims to determine if introducing hierarchy to a square lattice enhances the in-plane elastic properties and fracture toughness. The mode I and mode II fracture toughness of a hierarchical square lattice are determined using boundary layer analysis. The in-plane elastic properties of hierarchical square lattice are determined using finite element analysis and analytical calculations performed on a bar truss.

The increased nodal connectivity of the hierarchical square resulted in a higher shear modulus when compared to a nonhierarchical square lattice, as the response switched from bending dominated to stretching dominated. The mode II fracture toughness also increased considerably compared to the nonhierarchical square.

Keywords Fracture toughness, In-plane elastic properties, Lattice material, Linear elastic fracture mechanics.

Tekijä Akseli Lerailliez

Työn nimi Elastis-hauraan kaksiulotteisen hierarkkisen neliöhilan murtositkeys

Koulutusohjelma Koneenrakennustekniikka

Pääaine Kiinteän aineen mekaniikka

Vastuunopettaja/valvoja Apulaisprofessori Luc St-Pierre

Työn ohjaaja(t) Tohtorikoullutettava Milad Omid

Päivämäärä 15.07.2022 **Sivumäärä** 75 **Kieli** Englanti

Tiivistelmä

Hilamateriaaleja käytetään usein sovelluksissa, jotka vaativat materiaaliominaisuuksia joita ei ole saatavilla kiinteistä aineista. Hilamateriaalien tarjoamia materiaaliominaisuuksia käytetään erityisesti sovelluksissa, jotka vaativat kevyitä ja lujia materiaaleja. Lujat ja kevyet materiaalit mahdollistavat isompia rakenteita ja vähentävät kuljetuskustannuksia. Tavallisten hilojen materiaaliominaisuudet ovat tunnettuja, mutta hierarkkisten hilojen materiaaliominaisuuksia ei ole laajasti tutkittu. Erityisesti hierarkkisten hilojen murtositkeys on huonosti tunnettu vaikka murtumat ovat yleinen ongelma käytännön sovelluksissa.

Tämä diplomityö pyrkii määrittelemään parantaako hierarkia neliöhilan materiaaliominaisuuksia. Murtositkeys määritetään moodille I ja moodille II käyttäen rajakerros analyysiä. Elastiset ominaisuudet määritellään hierarkkiselle neliöhilalle elementtimenetelmällä ja analyyttisesti.

Hierarkkisen neliöhilan kasvanut solmu yhdistyneisyys johti korkeampaan liukumoduuliin verrattuna tavalliseen neliöhilaan. Hilan palkit muuttavat muotoaan venymällä taipumisen sijaan kasvaneen solmu yhdistyneisyyden ansiosta. Moodi II murtositkeys kasvoi huomattavasti verrattuna tavalliseen neliöhilaan.

Avainsanat Murtositkeys, Elastiset ominaisuudet, Hilamateriaali, Murtumismekaniikka

Contents

Preface.....	7
Symbols and abbreviations.....	8
Symbols	8
Operators.....	9
Abbreviations	9
1 Introduction	10
2 Literature review	13
2.1 Lattice material	13
2.2 Relative density	14
2.3 Bending and stretching dominated lattice materials	14
2.4 Nodal connectivity	15
2.5 In-plane elastic properties of lattice materials	16
2.6 Hierarchical lattice materials.....	16
2.7 Fracture toughness of lattice materials	18
2.8 Damage tolerance of lattice materials	22
3 In-plane elastic properties	23
3.1 Analytical modelling	23
3.1.1 Relative density	24
3.1.2 Young's modulus	25
3.1.3 Poisson's ratio.....	29
3.1.4 Shear modulus.....	29
3.2 Finite element modelling	38
3.2.1 Young's modulus	40
3.2.2 Poisson's Ratio.....	41
3.2.3 Shear modulus.....	41
3.3 Results	42
3.3.1 Young's modulus	43
3.3.2 Poisson's ratio.....	46
3.3.3 Shear modulus.....	47
4 Fracture toughness.....	52
4.1 Finite element modelling	52

4.2	Results	54
4.2.1	Grid dependency	54
4.2.2	Mode I fracture toughness	58
4.2.3	Mode I fracture locations	61
4.2.4	Mode II fracture toughness	64
4.2.5	Mode II fracture locations.....	66
4.3	Comparison to nonhierarchical square	69
5	Conclusions and outlook	72
6	References	73

Preface

I want to thank my supervisor Assistant Professor Luc-St Pierre for providing an interesting subject and for his support. I would also like to thank my advisor Doctoral Candidate Milad Omid for his support and for providing his Python scripts for fracture toughness simulations.

Finally, I want to thank my friend and family for their support during the writing of this master's thesis

Helsinki, 15 July 2022

Akseli Lerailliez

Symbols and abbreviations

Symbols

A	relative density scaling law coefficient
a	crack length
a_T	transition flaw size
B	Young's modulus scaling law coefficient
b	Young's modulus scaling law exponent
b_n	number of struts
C	shear modulus scaling law coefficient
c	shear modulus scaling law exponent
E	Young's modulus of the lattice material
E_s	Young's modulus of the solid
F	force vector
G	shear modulus of the lattice material
G_s	shear modulus of the solid
h	height of the unit cell
j	number of pin joints
K	Stress intensity factor
K_c	fracture toughness
K_s	stiffness matrix
l	strut length
m	the number of mechanisms
N	number of triangular elements
s	number of states of self-stress
T	bar force
t	in-plane thickness of struts
t_o	out-of-plane thickness of struts
w	width of the unit cell
ν	Poisson's ratio
ν_{ps}	plane strain Poisson's ratio
σ_f	tensile strength
σ_n	stretching induced axial stress
σ_m	bending induced stress
σ_t	axial stress on top face of element
σ_b	axial stress on bottom face of element
σ_{ys}	yield strength
τ	shear stress
ε	strain
ε_{ys}	yield strain
ε_f	fracture strain
θ	rotation
$\bar{\rho}$	relative density
W	virtual work

Operators

Σ_i	sum over index i
T	transpose

Abbreviations

LEFM	linear elastic fracture mechanics
FE	finite element

1 Introduction

Lattice materials are increasingly used in applications that require light and strong materials. The advantage of lattice materials is the wide range of stiffness, strength, and density that can be achieved. By controlling their architecture, lattice materials can be used in applications where solid materials do not offer the required material properties. This is visually represented on a material property space where lattice materials can be used to fill holes left by solid materials. For example, Figure 1 shows a material property space of Young's modulus as a function of density for various materials.

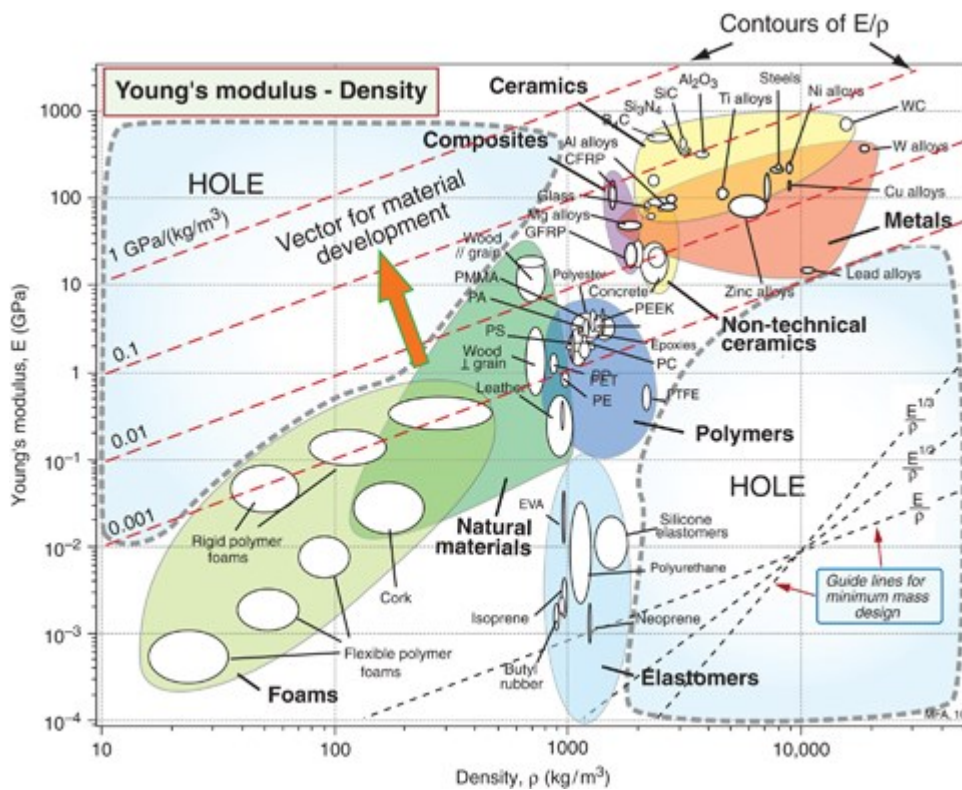


Figure 1: Material property space (Ashby, 2011).

Studies such as Fleck and Qiu (2007) have shown that lattice materials also have a high fracture toughness which is beneficial in structural applications. In many applications such as ships and bridges the limiting factor is resistance to fracture driving the search for materials with even higher fracture toughness. While relative Young's modulus or relative yield strength cannot exceed the relative density of the lattice, the fracture toughness is not limited to a theoretical maximum value (Hsieh et al., 2020).

Many biological materials such as wood or bone exhibit excellent fracture toughness. The high fracture toughness is largely attributed to the hierarchical design of biological materials (Launey and Robert, 2009). A study by Fan et al. (2008) predicted that introducing hierarchical design to hexagonal

lattice improves the fracture toughness encouraging further research into hierarchical lattice design.

The aim of this master's thesis is to determine the in-plane elastic properties and the fracture toughness of a hierarchical square lattice material to quantify how hierarchy can enhance this material property. The square lattice is selected because of its simplicity and the fracture toughness of the non-hierarchical square is known from previous studies. The hierarchical square is shown in Figure 2. Fracture toughness of various nonhierarchical topologies including the nonhierarchical square has been studied (Romijn and Fleck, 2007), but the fracture toughness of hierarchical lattices has not been extensively studied. In this master's thesis the fracture toughness and in-plane elastic properties of hierarchical square are determined using Finite Element (FE) simulations and the lattice material is assumed to be elastic-brittle. In addition, analytical equations are derived for the in-plane elastic properties. The cell walls of the lattice are assumed to contain no imperfections and have a constant tensile strength. The fracture toughness is determined for mode I and mode II. Failure pattern is investigated to assess if failure of a single strut results in macroscopic failure of the lattice.

The main finding of the thesis is that the increased number of struts in the hierarchical square changed the deformation mode from bending-dominated to stretching-dominated. This enhanced the shear modulus and mode II fracture toughness of the hierarchical square considerably.

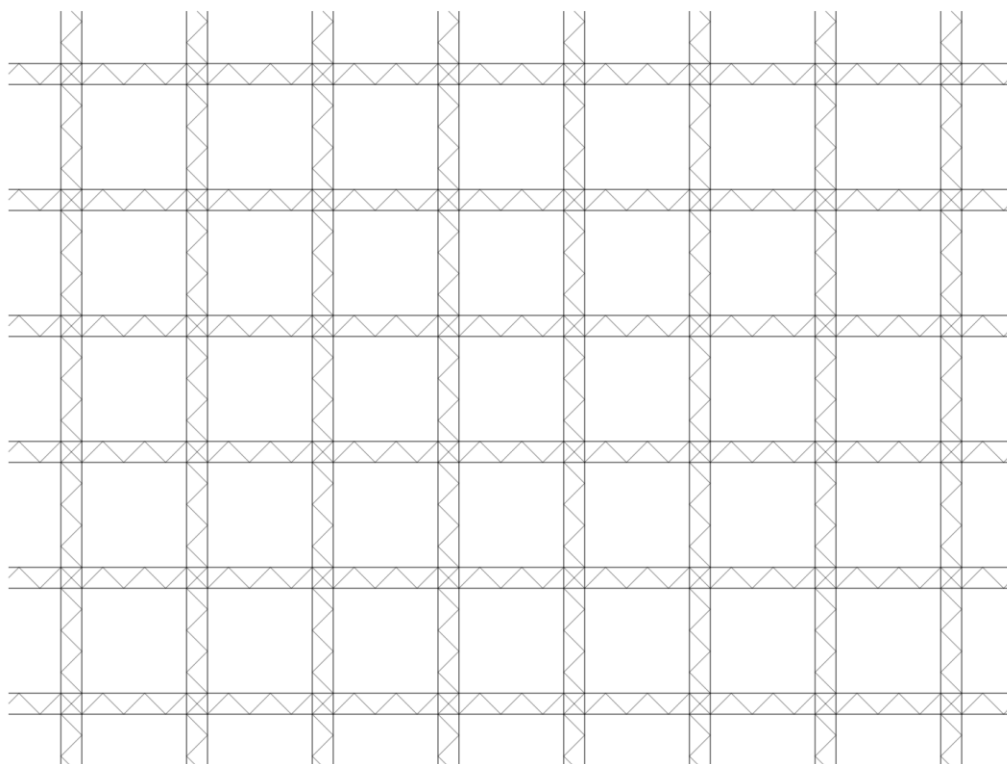


Figure 2: Hierarchical square lattice.

2 Literature review

The literature review aims to define lattice materials and to show how their material properties are presented. The deformation behaviours of lattice materials are examined and their effects on the in-plane elastic properties are quantified. Finally, methods for determining the fracture toughness of lattice materials are introduced.

2.1 Lattice material

Fleck et al. (2010, p. 2501) define lattice material as “a cellular, reticulated, truss or lattice structure made up of a large number of uniform lattice elements (e.g. slender beams or rods) and generated by tessellating a unit cell, comprised of just a few lattice elements, throughout space.” A lattice can behave as a material or as a structure depending on the wavelength of loading and number of lattice elements. Lattices behave as materials when the wavelength of loading is longer than lattice elements and the lattice contains a large number of lattice elements (Fleck et al., 2010). This means that lattices are considered at scales much larger than a single lattice element and consist of multiple unit cells.

Figure 3 shows unit cells for four different lattice topologies. Different unit cells are possible for the topologies shown, but unit cell must be chosen so that tessellating the unit cell results in a complete lattice.

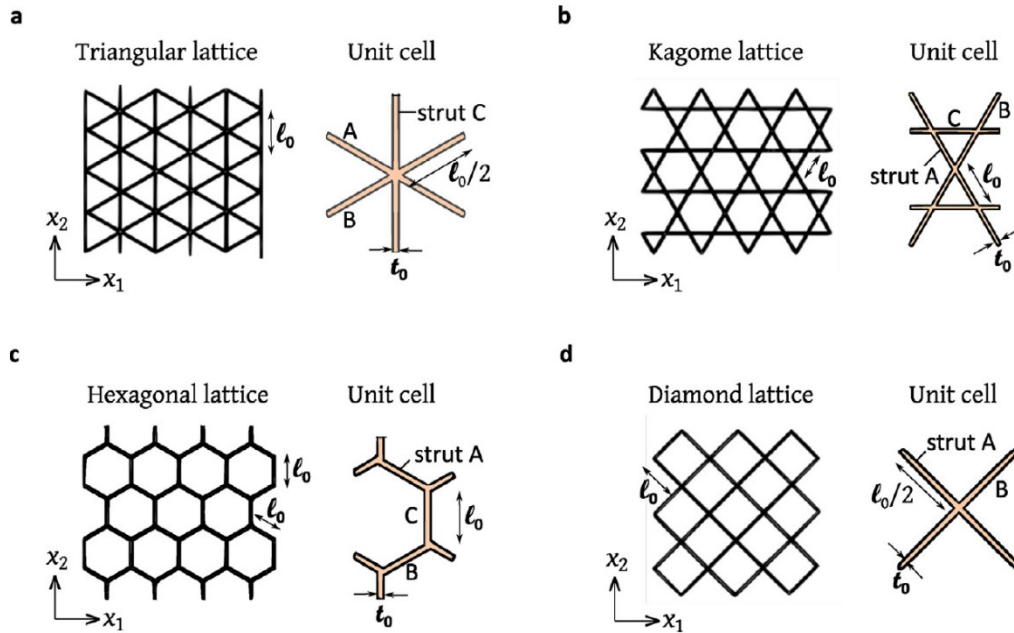


Figure 3: Different lattice topologies with corresponding unit cells (Tankasala et al., 2017).

Unit cells can be used to create the geometry of a large lattice by repeating the unit cell and to determine the material properties of the lattice material. The number of lattice elements in a unit cell is usually not sufficient to predict the response of a lattice material without the use of periodic boundary conditions. This requires constraining nodes at the boundary of the unit cell and will be examined in later sections 3.2 and 4.

2.2 Relative density

Relative density $\bar{\rho}$ is defined as the ratio of density of the lattice material to the density of the solid. When the relative density of the lattice material is low and the overlapping of the beam profiles at nodes is negligible the relative density is a function of the thickness and length of the struts given by:

$$\bar{\rho} = A \left(\frac{t}{l} \right) \quad (1)$$

where A is a coefficient that is dependent of the lattice topology (Fleck et al., 2010). Wang and McDowell (2004) have determined the coefficient A for various topologies, see Table 1.

Table 1: Scaling law coefficients and exponents for various topologies.

Topology	A	B	b	v	C	c
Square	2	1/2	1	$\frac{1}{2} v_s \bar{\rho}$	0.0625	3
Hexagonal	$2/\sqrt{3}$	3/2	3	1	0.375	3
Triangular	$2/\sqrt{3}$	1/3	1	1/3	0.125	1
Kagome	$\sqrt{3}$	1/3	1	1/3	0.125	1

2.3 Bending and stretching dominated lattice materials

Deshpande et al. (2000) divided lattice materials into two groups based on the deformation of the cell walls and treated lattice materials as a set of struts connected by pin joints. A mechanism seen on Figure 4(a) has no stiffness or strength. This is because the struts can rotate resulting in the cell collapsing if loaded. If the pin joints of the mechanism are locked the struts are no longer free to rotate. When load is applied bending moment is induced on the joints causing the struts to bend meaning that the deformation is bending-dominated. A structure can be seen in Figure 4(b). In a structure the struts are not able to rotate and instead carry tensile or compressive loads when a load is applied. This results in the structure having rigidity and it is deforming by stretching of the struts. Locking the joints in a structure has negligible

effect on the stiffness or strength as the deformation is still stretching-dominated.

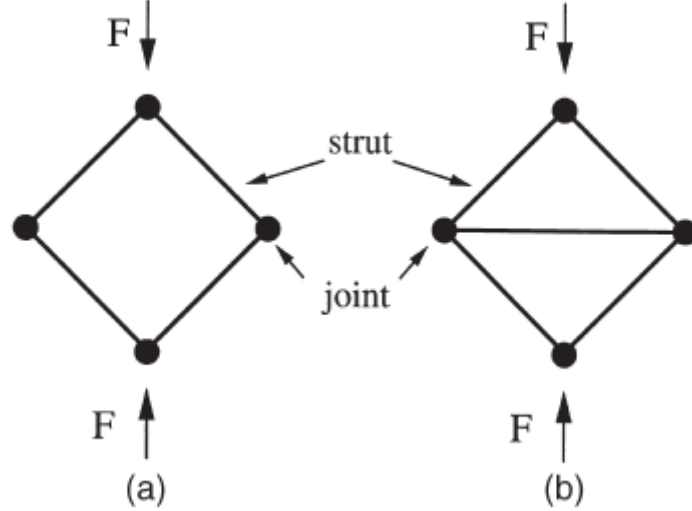


Figure 4: (a) A mechanism, (b) a structure (Deshpande et al., 2000).

There is considerable difference in material properties between bending-dominated and stretching-dominated lattices. Using foams as an example it is noted that, “foams that are stretching-dominated are more efficient from a weight standpoint; for example, a stretching-dominated foam is expected to be about ten times as stiff and about three times as strong as a bending-dominated foam for a relative density $\bar{\rho} = 0.1$.” (Deshpande et al., 2000, p. 1035).

2.4 Nodal connectivity

Nodal connectivity is defined as the number of struts connected to each node of the lattice. Nodal connectivity determines whether the cell walls deform by stretching or bending. As stretching-dominated lattices will be stiffer and stronger compared to bending-dominated lattices it can be beneficial to define criteria for rigidity of a cell that comprises of pin jointed struts. Maxwell (1864) presented the following equations that need to be satisfied for the cell to be rigid and statically determinate for 2D and 3D:

$$b_n = 2j - 3 \quad (2)$$

$$b_n = 3j - 6 \quad (3)$$

respectively. In Equations (2) and (3) b_n is the number of struts and j is the number of pin joints. Satisfying equations (2) or (3) is required for rigidity and statical determinacy, but rigidity is not guaranteed even if the equation

is satisfied. This can be seen by examining the generalization of Equation (3) given by Calladine (1978):

$$b_n - 3j + 6 = s - m, \quad (4)$$

where s is the number of states of self-stress and m is the number of mechanisms. A rigid cell should contain no states of self-stress or mechanisms (Deshpande et al., 2000). By comparing Equations (4) and (3) it can be seen that satisfying equation (3) does not guarantee that there is no mechanisms or state of self-stress but instead that $s = m$.

2.5 In-plane elastic properties of lattice materials

The in-plane stiffness of lattices can be represented using a power-law equation:

$$\frac{E}{E_s} = B \bar{\rho}^b, \quad (5)$$

where E/E_s is the Young's modulus of the lattice material divided by the Young's modulus of the solid, i.e. the relative Young's modulus (Fleck et al., 2010). The coefficient B and exponent b are shown for various topologies in Table 1. Similarly, the power-law equation for the relative shear modulus is:

$$\frac{G_{12}}{E_s} = C \bar{\rho}^c. \quad (6)$$

The exponents b and c are indicative of the lattice's deformation behaviour. For stretching-dominated lattices, $b = c = 1$ and for bending-dominated lattices, $b = c = 3$ (Fleck et al., 2010). Table 1 shows that the triangular lattice is stretching-dominated and the hexagonal lattice is bending-dominated. The deformation behaviour of the square lattice depends on the loading. When loaded in tension or compression parallel to the struts the deformation is stretching-dominated and when loaded in shear the deformation is bending-dominated.

The Poisson's ratio ν is given in Table 1 and is usually independent of relative density and Poisson's ratio of the solid for low relative densities where Euler-Bernoulli beam theory applies (Fleck and Qiu, 2007). Exception to this is the square topology where the unit cell consists of only two struts. In this case the Poisson's ratio is entirely dependent on the Poisson's effect of the solid and therefore must be considered.

2.6 Hierarchical lattice materials

A hierarchical lattice contains multiple lattice structures on different length scales. This means that the struts forming the coarse lattice contain a finer scale lattice. This is illustrated in Figure 5 for a lattice containing two levels of hierarchy.

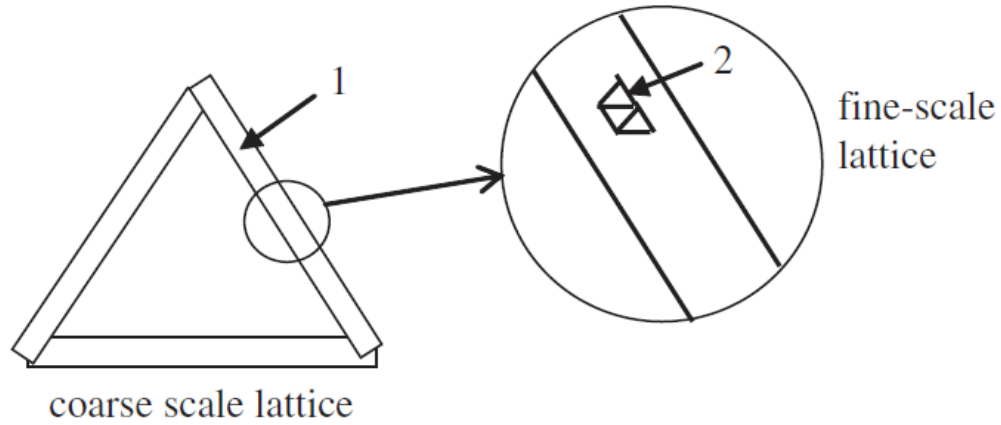


Figure 5: Hierarchical lattice containing two length scales (Fleck et al., 2010).

One of the benefits of smaller length scales is presented by Kooistra et al. (2007) who studied the compressive strength of a truss structure containing hierarchical struts. As the buckling strength increases with decreasing strut length, using a smaller scale lattice (with shorter struts) significantly increased the compressive strength of the hierarchical truss structure compared to the nonhierarchical lattice.

Increase in energy absorption is also a benefit of hierarchical design. Increased energy absorption is beneficial for example, in the automotive industry to increase crashworthiness. Tsang et al. (2019) experimentally investigated the energy absorption of a tubular structure inspired by skeletal muscle tissue. They found that the energy absorption increased by 172% when three levels of hierarchy were introduced. They also suggested that the energy absorption can be increased even further by introducing more levels of hierarchy.

Fleck et al (2010) divided hierarchical lattices into three groups. First of these groups is stretching-stretching structures. In stretching-stretching structures both lattices are stretching-dominated, and the rigidity of the structure is high. This requires sufficient nodal connectivity for both structures. Bending-bending structures are the opposite of stretching-stretching structures. In Bending-bending structures both lattice structures are bending-dominated resulting in low rigidity. This can be beneficial for damage tolerance as deflections create only small stresses in the structure compared to stretching-stretching structures. Finally, the intermediate category is the

stretching-bending structure where one of the lattices is stretching-dominated and the other one is bending-dominated.

In cases where the coefficients and exponents of the scaling laws are known for each topology of the hierarchical lattice the effective Young's modulus can be calculated by combining the expressions for each topology. For example, for a hierarchical lattice containing two topologies the effective modulus for the finer lattice can be calculated first

$$E_f = B_f \bar{\rho}_f^{b_f} E_s \quad (7)$$

and E_f can be used as the Young's modulus of the coarse lattice solid resulting in equation

$$E_c = B_c \bar{\rho}_c^{b_c} E_f = B_c \bar{\rho}_c^{b_c} B_f \bar{\rho}_f^{b_f} E_s, \quad (8)$$

where subscripts f and c denote the finer and coarse lattices, respectively (Fleck et al., 2010).

2.7 Fracture toughness of lattice materials

Irwin (1957) proposed the following criterion for failure of a cracked specimen

$$K \geq K_c, \quad (9)$$

where K is the stress intensity factor and K_c is the fracture toughness. The stress intensity factor and fracture toughness in the equation above do not have subscripts, but fracture toughness is loading mode dependent. Fracture toughness is the critical stress intensity factor that results in crack growth. While the stress intensity factor is typically independent of material, fracture toughness is a material property. For elastic-brittle lattices, their fracture toughness is given by:

$$\frac{K_c}{\sigma_f \sqrt{l}} = D \bar{\rho}^d, \quad (10)$$

where D is a scaling coefficient, d is a scaling law exponent, σ_f is the tensile strength of the cell wall material, and l is cell wall length (Fleck and Qiu, 2007). For elastoplastic lattices, an additional term is included and the power law becomes:

$$\frac{K_{JIC}}{\sigma_{ys}\sqrt{l}} \left(\frac{\varepsilon_{ys}}{\varepsilon_f} \right)^{\frac{p+1}{2p}} = D\bar{\rho}^d, \quad (11)$$

where σ_{ys} is the yield strength, ε_{ys} is the yield strain, ε_f is the fracture strain, and p is the strain hardening exponent (Hsieh et al., 2020).

Various methods for determining the fracture toughness of lattice materials exists. The first methods used analytical formulas and later methods relied on FE simulations to determine the fracture toughness.

One of the first studies of lattice material fracture toughness was conducted by Maiti et al. (1984). They derived the mode I fracture toughness K_{IC} for an isotropic brittle-elastic foam analytically. They calculated the Linear Elastic Fracture Mechanics (LEFM) stress field for a continuous material equivalent to the lattice material. The continuous problem is then transformed into a discrete problem by calculating the forces and moments acting on the unit cell struts from the stress field. The fracture toughness is then the value of stress intensity K_I corresponding to the tensile strength of the solid.

One of the methods for determining the fracture toughness using FE simulation is to simulate a finite lattice containing a crack and relate the loading on the boundary to a known LEFM equation corresponding to the loading and crack. For example, the mode I stress intensity factor for an infinitely large plate containing an edge crack is given by equation

$$K_I = 1.12\sigma_{\infty}\sqrt{\pi a}, \quad (12)$$

where σ_{∞} is the applied stress and a is the crack length. Fracture toughness is then the stress intensity at which any of the lattice beams reach the maximum tensile fracture strength of the solid. For this method to produce accurate value of fracture toughness the following inequality must be satisfied

$$b \gg a \gg l, \quad (13)$$

where b is the lattice length, a is the crack length, and l is the cell wall length (Lippman et al., 2007).

The method described above was further improved by Schmidt and Fleck (2001) using continuum fracture mechanics. Boundary layer method uses a finite lattice containing a crack that is implemented by removing beams. The stress field is then calculated for an equivalent continuum material. From the stress field, the strain components can be calculated using Hooke's law and then integrated to obtain a displacement field. The following equations from Williams (1957), expressed using polar coordinates originating from the crack tip of a crack located on the negative x_1 - axis, give the displacement field for an isotropic material loaded in mode I or mode II

$$u_1 = \frac{K_I}{2G\sqrt{2\pi}} r^{\frac{1}{2}} (\kappa - \cos \theta) \cos \frac{\theta}{2} + \frac{K_{II}}{2G\sqrt{2\pi}} r^{\frac{1}{2}} (\kappa + 2 + \cos \theta) \sin \frac{\theta}{2} \quad (14)$$

and

$$u_2 = \frac{K_I}{2G\sqrt{2\pi}} r^{\frac{1}{2}} (\kappa - \cos \theta) \sin \frac{\theta}{2} - \frac{K_{II}}{2G\sqrt{2\pi}} r^{\frac{1}{2}} (\kappa - 2 + \cos \theta) \cos \frac{\theta}{2}, \quad (15)$$

where κ is

$$\kappa = \frac{3 - \nu_{ps}}{1 + \nu_{ps}}, \quad (16)$$

and ν_{ps} is the Poisson's ratio under plane strain constraints. Equations (14) and (15) show that a material can also be loaded in two modes simultaneously as the displacement field can be calculated by adding the contribution of each stress intensity mode. The displacement field depends on material properties in addition to stress intensity factor meaning that the effective material properties of the lattice must be determined. The displacement field is then applied to the outer boundary of the lattice. The stresses in the lattice beams are solved using FE simulations and the fracture toughness corresponds to the stress intensity where the tensile strength of the solid is reached. For boundary layer analysis the condition for crack length is:

$$a \gg l \quad (17)$$

(Lipperman et al., 2007). Equation (17) shows that boundary layer analysis does not require the lattice domain to be significantly larger than the crack length enabling the use of smaller lattices. This leads to reduced computational time.

Table 2 shows the scaling law coefficients and exponents for various topologies obtained using the boundary layer analysis. It should be noted that the Kagome lattice has a very high fracture toughness. Fracture toughness is highly dependent on the exponent d and only the Kagome topology has a value of d below one.

Table 2: Scaling parameters for the fracture toughness of brittle lattices.

Topology	Mode 1		Mode 2		Reference
	D	d	D	d	
Hexagonal	0.80	2	0.37	2	Fleck and Qiu (2007)
	0.90	2	0.41	2	Romijn and Fleck (2007)
Triangular	0.50	1	0.38	1	Fleck Qiu (2007)
	0.61	1	0.40	1	Romijn and Fleck (2007)
Kagome	0.21	0.50	0.13	0.50	Fleck and Qiu (2007)
	0.21	0.50	0.12	0.50	Romijn and Fleck (2007)
Square	0.28	1	0.12	1.50	Romijn and Fleck (2007)
Diamond	0.22	1	0.23	1	Romijn and Fleck (2007)

All the methods presented above are based on LEFM. LEFM applies only when the plastic zone is small, approximately an order of magnitude smaller than the crack length. For ductile materials that experience plastic deformation, boundary layer analysis is only suitable when displacements are small.

If the size of the plastic deformation is large nonlinear elastic fracture mechanics approach based on the J-integral is needed. The J-integral is the non-linear elastic energy release rate. Hsieh et al. (2020) investigated the fracture toughness of 2D isotropic lattices using J-integral based FE calculations. They also calculated the R-curve showing that triangular lattice has a rising R-curve meaning that the lattice material toughens as the crack progresses. In contrast, the hexagonal lattice does not toughen and exhibits brittle failure. The difference in failure behavior is attributed to the size of the plastic zone. Table 3 shows the Mode I fracture toughness for three topologies obtained by Hsieh et al. (2020). The strain hardening exponent $p=16$ corresponds to titanium alloy (Ti-6Al-4 V).

Table 3: Scaling parameters for the mode I fracture toughness of elastoplastic lattices.

Topology	D			d
	$p = 10$	$p = 16$	$p = \infty$	
Triangular	0.42	0.57	0.38	1
Kagome	0.16	0.22	0.09	0.5
Hexagonal	0.5	0.47	0.22	2

To validate these analytical and numerical methods, experimental studies on the fracture toughness of lattice materials have been conducted. Gu et al. (2018) conducted an experimental study on the mode I fracture toughness of a triangular lattice. The fracture toughness was experimentally measured using an edge cracked specimen and compared against boundary layer FE analysis. They found that the experimental fracture toughness was in good

agreement with the boundary layer analysis when the specimen is large compared to the unit cell size.

Finally, it should be noted that there is a statistical component to the fracture of brittle lattices. Huang and Gibson (1991) investigated the fracture toughness of brittle foams and assumed that the tensile strength of the lattice struts follows the Weibull distribution. They found that the fracture toughness varies with respect to the Weibull modulus and the unit cell size.

2.8 Damage tolerance of lattice materials

Damage tolerance describes how sensitive a lattice topology is to cracks. Fleck and Qiu (2007) investigated the damage tolerance of hexagonal, triangular, and Kagome topologies using FE simulation of a center cracked square lattice with side length of 200 unit cells. They found that the hexagonal and triangular topologies are not very damage tolerant resulting in the fracture strength being a function of crack length when the length of the crack is two cells or more. For Kagome topology the fracture strength remained independent of the crack length for longer cracks until a transition flaw size was reached. Transition flaw size is the crack length at which the fracture strength begins to be a function of crack length and the fracture strength is predicted by LEFM.

This is illustrated in Figure 6, where the tensile fracture strength for a center cracked lattice is plotted as a function of the flaw size and, where the transition flaw size is denoted by a_T . For cracks longer than the transition flaw size the tensile fracture strength is given by equating the stress intensity factor to the fracture toughness of the lattice.

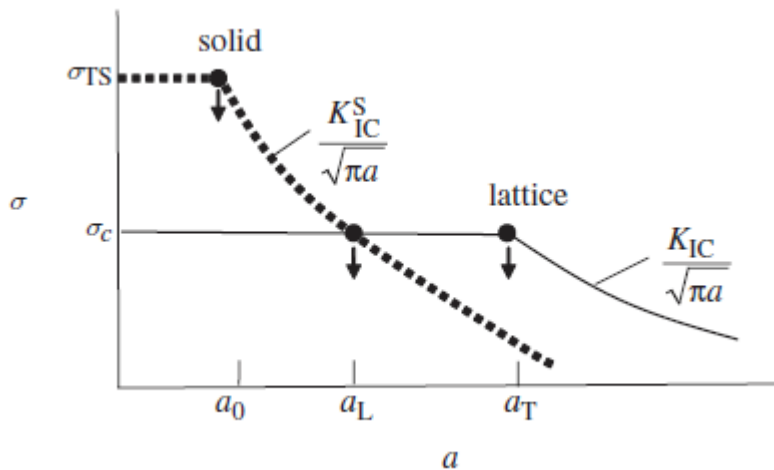


Figure 6: Damage tolerance for a center cracked specimen (Fleck et al., 2010).

3 In-plane elastic properties

First the unit cell of a hierarchical square is defined, and its relative density calculated to give context to the methods that follow. Two methods are given for determining the in-plane elastic properties, one corresponding to FE simulations and one to analytical calculations.

3.1 Analytical modelling

Analytical predictions are given for the Young's modulus, Poisson's ratio, and shear modulus of the lattice material. The predictions are calculated using the principle of virtual work. The analytical equations are derived using a pin jointed truss structures where each strut is represented by a bar.

The hierarchical lattice investigated in this master's thesis is a combination of two topologies. The coarse lattice is square, and the struts of the square lattice consist of triangular elements. The triangular struts are at a 45° angle with respect to the square lattice struts. The orientation of the lattice is $0/90^\circ$. The nodal connectivity is not constant and instead the centre of the unit cell contains an area of high nodal connectivity while elsewhere the nodal connectivity is four. Figure 7 shows the lattice and the dotted lines indicates the unit cell that is used in the following sections. It is important to note that for the hierarchical square the material properties depend not only on the strut length and thickness, but also on the number of struts in the finer triangular lattice.

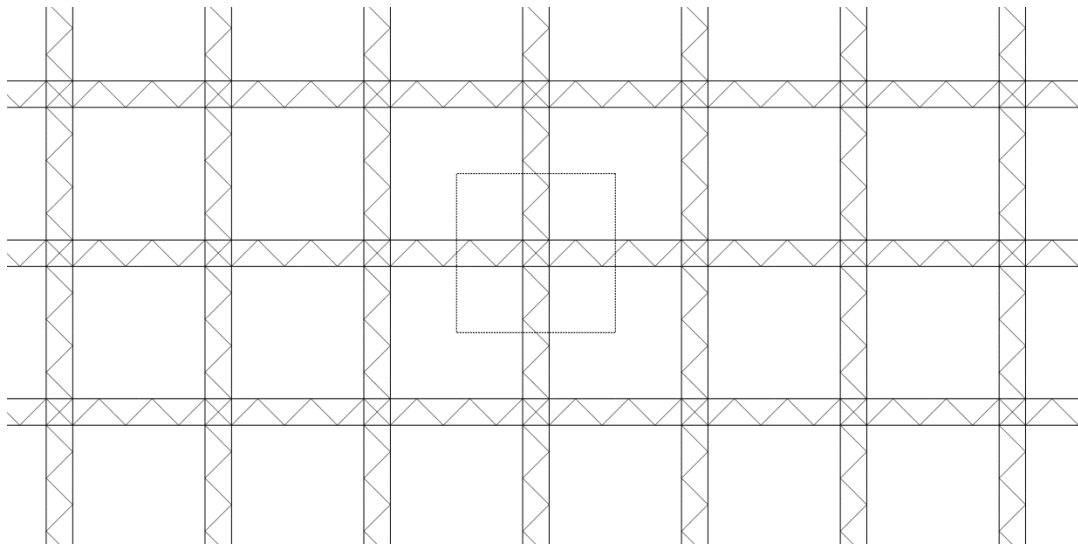


Figure 7: Unit cell selection.

3.1.1 Relative density

Relative density is defined as the ratio of the density of the lattice material to the density of the solid. For a planar lattice this can be expressed using area with the following equation

$$\bar{\rho} = \frac{A_l}{A_{tot}}, \quad (18)$$

where A_l is the area occupied by the unit cell struts and A_{tot} is the total area of the unit cell.

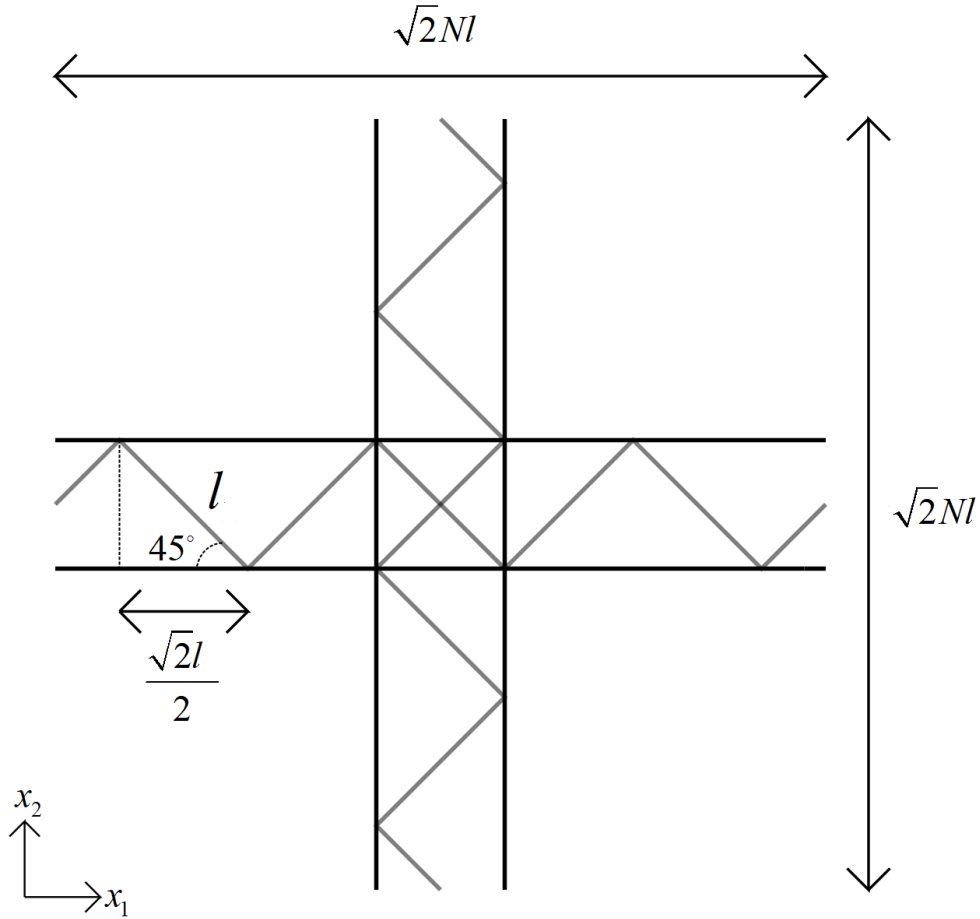


Figure 8: Dimensions of the unit cell.

Figure 8 shows the dimensions of the unit cell. The square lattice is shown in black, and the triangular lattice is shown in grey and contains trusses of length l . A variable N can be introduced as the number of triangular elements

in x_1 and x_2 directions. For example, the unit cell in Figure 8 has $N = 3$ as it contains three triangular elements in x_1 and x_2 directions. Each triangular element contains two inclined struts, and the continuity of the lattice structure is ensured as even number of inclined struts is required in x_1 and x_2 directions for a continuous lattice. This means that the value of N can only be a non-negative integer excluding zero.

The unit cell dimensions are symmetric, and the height h and width w of the unit cell can be calculated using the number of triangular elements and this gives:

$$w = h = \sqrt{2}Nl. \quad (19)$$

The total area of the unit cell can be calculated by multiplying the sides of the unit cell which returns:

$$A_{tot} = wh = (\sqrt{2}Nl)^2. \quad (20)$$

The area occupied by the lattice can be calculated by adding the area of the trusses. The number of triangular elements is given by N and the square lattice always contains four trusses that span the entire unit cell width or height resulting in the following equation:

$$A_l = 4Nlt + 4\sqrt{2}Nlt. \quad (21)$$

Finally, substituting these results in Equation (18) gives the relative density:

$$\bar{\rho} = \frac{2(1+\sqrt{2})}{N} \frac{t}{l}. \quad (22)$$

3.1.2 Young's modulus

The stiffness of the lattice material can be represented by Young's modulus that is determined using the equation

$$E = \frac{\sigma_{ii}}{\varepsilon_{ii}}. \quad (23)$$

The Young's modulus is referred to as E due to symmetry of the unit cell $E_{11} = E_{22} = E$ and intermediate loading orientations are not examined.

The analytical prediction of the Young's modulus is made by assuming that the load is carried only by the struts parallel to the loading direction and the high nodal connectivity center of the unit cell. The validity of this assumption is assessed in section 3.3.1. These two parts are shown in Figure 9. The struts colored blue mark the struts parallel to loading and are denoted by

superscript A in the calculations. The struts coloured red mark the unit cell center and are denoted by superscript B in the calculations. In the analytical calculations the Young's modulus calculated is E_{22} , but due to symmetry of the unit cell the calculations are identical for E_{11} .

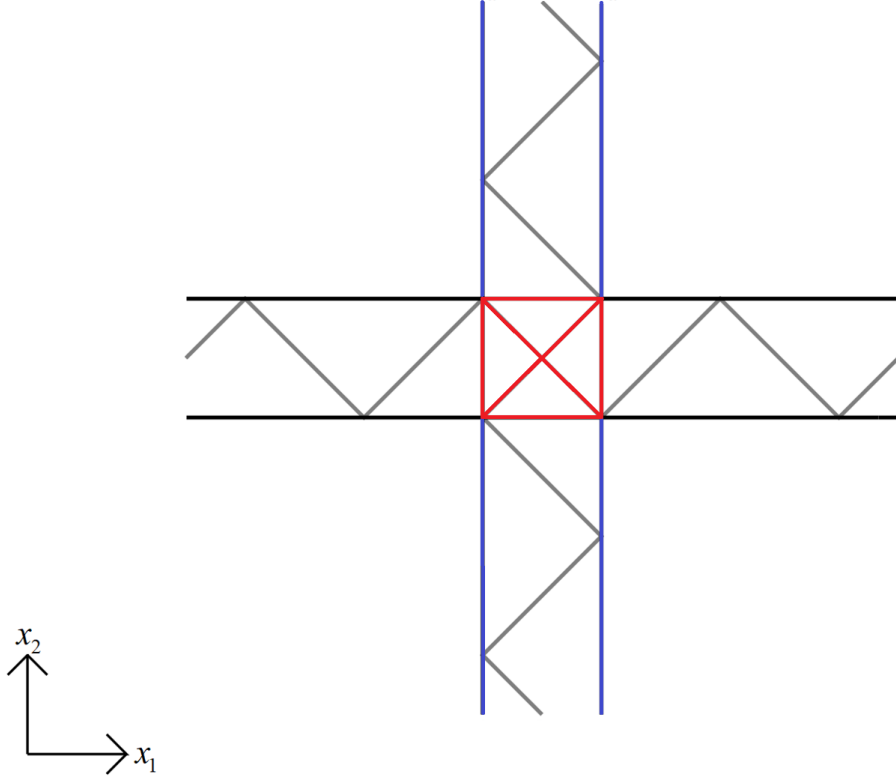


Figure 9: Division of the response.

There are always two struts parallel to the loading direction when the unit cell is loaded in x_1 or x_2 directions. Using this information, the strain component parallel to the load is given by:

$$\varepsilon_{22}^A = \frac{\sigma}{E_s} = \frac{P}{2tt_oE_s}, \quad (24)$$

where P is the force applied. The displacement can be calculated by multiplying the strain with the length of the struts, which is the unit cell length subtracted by the center length, and this gives:

$$u_2^A = \frac{P}{2tt_oE_s} (2N - 1) \frac{\sqrt{2}}{2} l. \quad (25)$$

Next the displacement from the center must be calculated. Figure 10 shows the unit cell centre with node numbers and loading. Upward force is applied to nodes 3 and 4. Boundary conditions are for node 1 $u_1 = u_2 = 0$ and for node 2 $u_2 = 0$. The length of the diagonal struts is l .

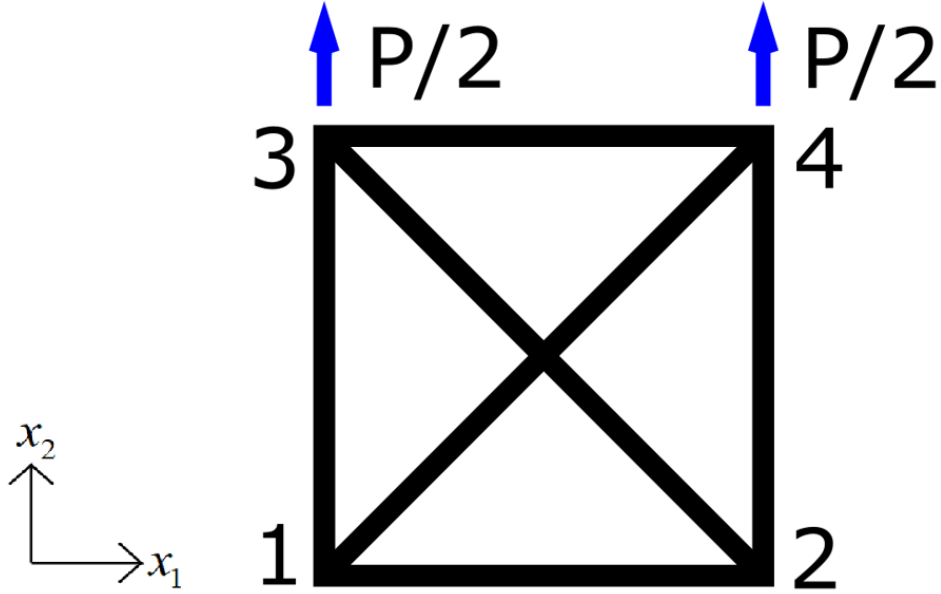


Figure 10: Unit cell center.

Due to the static indeterminacy of the center, information about the strut stiffness is required and the following virtual work expression is used

$$\delta W = -\delta \mathbf{u}^T (\mathbf{K}_s \mathbf{u} - \mathbf{F}) = 0, \quad (26)$$

where W is the virtual work, \mathbf{u} is the displacement vector, \mathbf{K}_s is the stiffness matrix, and \mathbf{F} is the force vector. The displacement vector is given by:

$$\mathbf{u}^T = [u_1^2 \quad u_1^3 \quad u_1^4 \quad u_2^3 \quad u_2^4], \quad (27)$$

where the superscript denotes the node number. The force vector is given by:

$$\mathbf{F}^T = [0 \quad 0 \quad 0 \quad P/2 \quad P/2]. \quad (28)$$

The stiffness matrix is given by:

$$\mathbf{K}_s = \frac{AE_s}{2l} \begin{bmatrix} 1+2\sqrt{2} & -1 & 0 & 1 & 0 \\ -1 & 1+2\sqrt{2} & -2\sqrt{2} & -1 & 0 \\ 0 & -2\sqrt{2} & 1+2\sqrt{2} & 0 & 1 \\ 1 & -1 & 0 & 1+2\sqrt{2} & 0 \\ 0 & 0 & 1 & 0 & 1+2\sqrt{2} \end{bmatrix}, \quad (29)$$

where A is the cross-sectional area of the bars. Using the principle of virtual work stating that $\delta W = 0 \forall \delta \mathbf{u}$ results in a linear equation system that is solved using a Mathematica script. This gives the following equation for the node displacement in x_2 -direction for nodes 3 and 4

$$u_2^B = \frac{(1+2\sqrt{2})lP}{4(2+\sqrt{2})tt_oE_s}. \quad (30)$$

The total strain in the loading direction includes both displacements and is given as:

$$\varepsilon_{22} = \frac{u_2^A + u_2^B}{h} = \frac{(4N - \sqrt{2} + 1)P}{8E_sNtt_o}. \quad (31)$$

The stress component corresponding to the load P is given by:

$$\sigma_{22} = \frac{P}{wt_o} = \frac{P}{\sqrt{2}Nlt_o}. \quad (32)$$

The Young's modulus can be calculated by substituting Equations (31) and (32) in (23), which returns:

$$E = \frac{4\sqrt{2}E_s t}{(4N - \sqrt{2} + 1)l}. \quad (33)$$

This result can be expressed as a function of relative density using Equation (22). After normalising the equation, the relative Young's modulus becomes:

$$\frac{E}{E_s} = \frac{2N(2 - \sqrt{2})\bar{\rho}}{4N - \sqrt{2} + 1} = \frac{0.2929N\bar{\rho}}{N - 0.1036}. \quad (34)$$

As the number of triangular elements N is increased, the Young's modulus converges to a solution where only the struts parallel to the loading direction are considered. This is because increasing N increases the length scale of the unit cell, whereas the center remains constant, which reduces its effect on the stiffness of the lattice.

3.1.3 Poisson's ratio

The Poisson's ratio is defined as

$$v = -\frac{\varepsilon_{11}}{\varepsilon_{22}}, \quad (35)$$

and due to symmetry of the unit cell $v = v_{12} = v_{21}$. Poisson's ratio is predicted using an assumption that the high nodal connectivity centre of the unit cell is mainly responsible of the strain transverse to the loading direction. This is assumed because the centre contains struts in compression transverse to the loading direction resulting in high stresses in the diagonal bars.

The equation system from section 3.1.2 can be used to solve the displacement transverse to the forces P . The displacement of each node to x_1 -direction is as follows

$$u_1^1 = u_1^3 = 0 \quad (36)$$

and

$$u_1^2 = u_1^4 = -\frac{Pl}{4(2 + \sqrt{2})tt_oE_s}, \quad (37)$$

where the superscript denotes the node number.

With the displacement known, the strain component in the transverse direction can be calculated. This is done by dividing the displacement by the width of the unit cell (see Equation (19)) and this gives:

$$\varepsilon_{11} = \frac{u_1^2 - u_1^1}{\sqrt{2}Nl} = \frac{u_1^4 - u_1^3}{\sqrt{2}Nl} = \frac{P(1 - \sqrt{2})}{8E_sNtt_o}. \quad (38)$$

The strain component parallel to the loading direction is given by Equation (31). Substituting Equations (31) and (38) in (35) gives the Poisson's ratio:

$$v = \frac{\sqrt{2} - 1}{4N - \sqrt{2} + 1} = \frac{0.1036}{N - 0.1036}. \quad (39)$$

3.1.4 Shear modulus

Shear modulus is defined as the ratio of shear stress to shear strain and is expressed as:

$$G_{12} = \frac{\tau_{12}}{\varepsilon_{12}}. \quad (40)$$

The first step to calculate the shear modulus is to determine the forces induced in the outer bars by the shear stress. Due to symmetry, there only two different forces as shown in Figure 11 for a $N = 1$ unit cell. The absolute value of the bar force does not depend on N , but each incremental increase of N changes the sign (see Figure 11 and Figure 13).

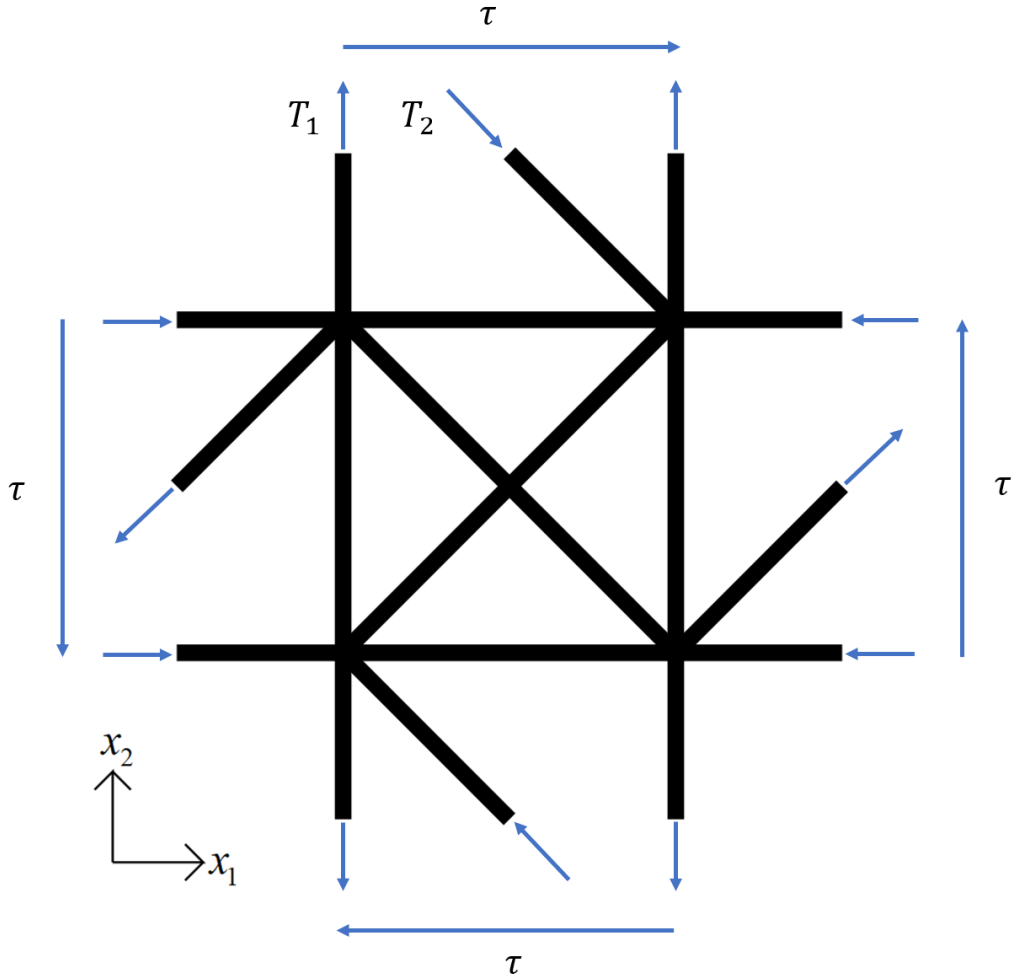


Figure 11: Shear loading and internal bar forces.

The bar forces T_1 and T_2 can be solved by forming the following equilibrium equations in the x_1 and x_2 -directions

$$\frac{\sqrt{2}}{2} T_2 = \tau t_o w \quad (41)$$

and

$$-\frac{\sqrt{2}}{2}T_2 + 2T_1 = 0. \quad (42)$$

Solving Equations (41) and (42) gives the forces in the bars

$$T_1 = \frac{\tau t_o w}{2} = \frac{P}{2} \quad (43)$$

and

$$T_2 = \sqrt{2}\tau t_o w = \sqrt{2}P, \quad (44)$$

where P denotes the shear force applied and t_o is the out-of-plane depth.

With the forces in the outer bars known the forces in the rest of the bars can be calculated to form virtual work expressions. The following virtual work equation will be used to calculate the displacements

$$u_1 + u_2 = \sum_i^{bars} \frac{l_i}{E_s A} T_i^0 T_i^0 (P = 1), \quad (45)$$

where T_i^0 is the actual force in each bar and $T_i^0 (P = 1)$ is the bar force from the test load corresponding to stress components τ_{12} and τ_{21} so that both shear forces are unity. u_1 is the displacement to x_1 -direction induced by shear stress τ_{21} that results in an angle between the top and bottom surfaces of the unit cell, similarly u_2 is the displacement to x_2 -direction corresponding to shear stress τ_{12} . Equation (45) shows that the forces in the bars due to the actual load and test load are equal, except P is set to unity for the test load. This means that it is not necessary to consider if a bar is in tension or compression in the virtual work expressions simplifying the calculations. The virtual work expression of the unit cell is divided into three parts shown in Figure 12 consisting of the inclined bars marked in green, straight bars in blue, and the unit cell center in red. Expressing Equation (45) as a sum of the virtual work parts gives:

$$u_1 + u_2 = W^{inclined} + W^{straight} + W^{center}. \quad (46)$$

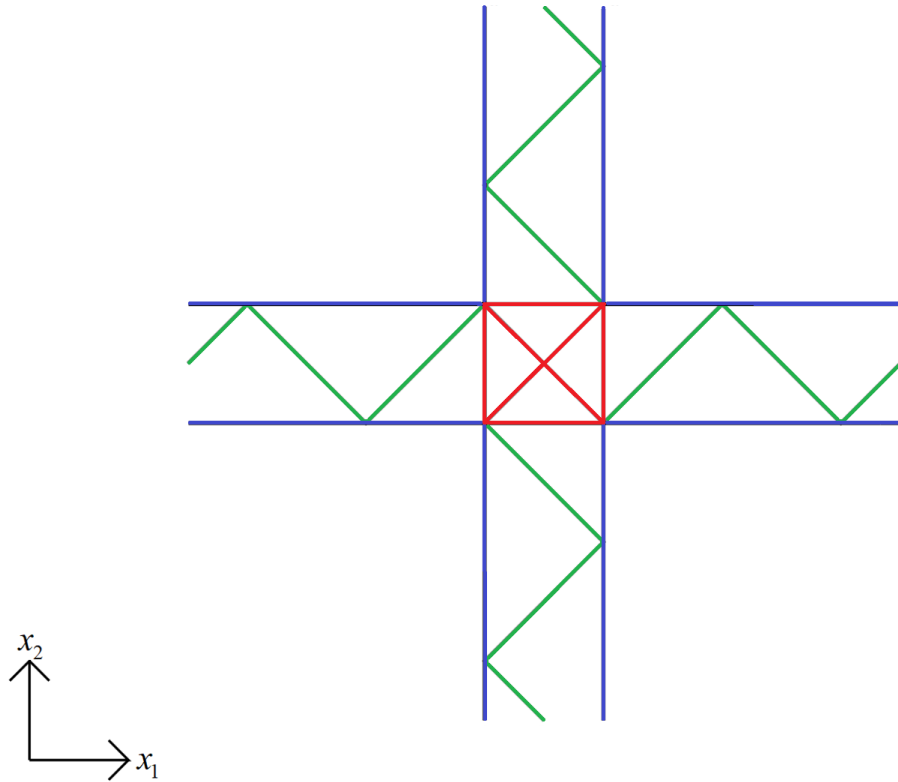


Figure 12: Division of virtual work expressions.

Next the bar forces in the unit cell can be calculated. The joints are numbered in Figure 13. The bar forces are calculated by forming equilibrium equations for each joint. The equations are listed in Table 4 and the bar forces are given in Table 5.

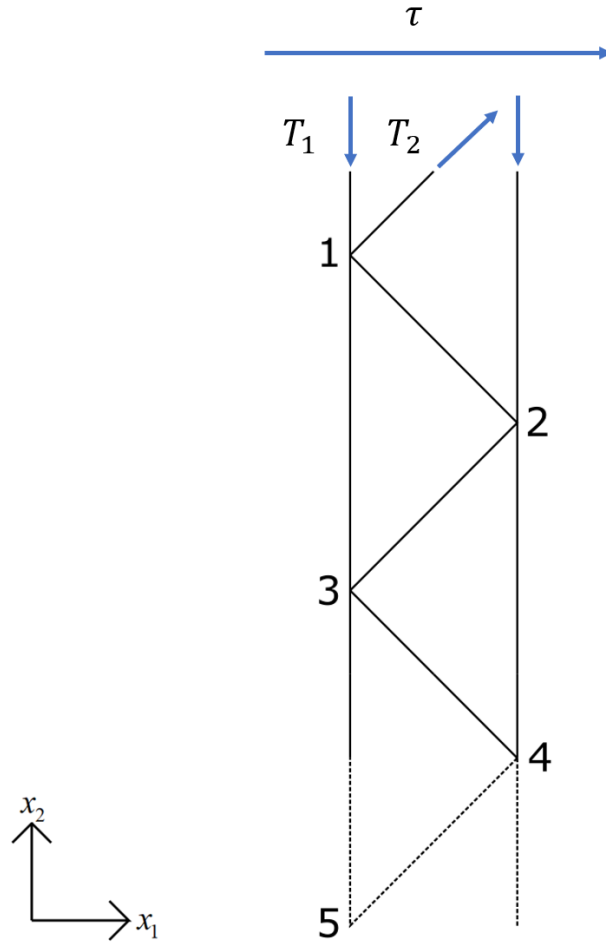


Figure 13: Numbering of the joints.

Table 4: Joint calculations

Joint	x_1 -direction	x_2 -direction
1	$P + \frac{\sqrt{2}}{2} T_{12} = 0$	$-\frac{P}{2} + P - T_{13} - \frac{\sqrt{2}}{2} T_{12} = 0$
2	$P - \frac{\sqrt{2}}{2} T_{23} = 0$	$-P - \frac{P}{2} - \frac{\sqrt{2}}{2} T_{23} - T_{24} = 0$
3	$P + \frac{\sqrt{2}}{2} T_{34} = 0$	$\frac{3}{2}P + P - \frac{\sqrt{2}}{2} T_{34} - T_{35} = 0$

Table 5: Bar forces.

Bar	Force
T_{12}	$-\sqrt{2}P$
T_{13}	$\frac{3}{2}P$
T_{23}	$\sqrt{2}P$
T_{24}	$-\frac{5}{2}P$
T_{34}	$-\sqrt{2}P$
T_{35}	$\frac{7}{2}P$

Calculating the bar forces using only three joints is enough as the structure is repeating. Table 5 shows that the straight bars on the left are in tension except for the first bar, the inclined bars in the middle have constant absolute values of force while the sign changes every other bar, and the straight bars on the right side are in compression.

The virtual work expression for the inclined bars can be calculated first as this is the simplest expression due to the constant absolute value of bar forces. Each inclined bar is of length l , each incremental increase of N adds 4 bars, and the center of the unit cell contains 2 inclined bars. Using this information, the contribution to virtual work is given by:

$$\begin{aligned}
W^{inclined} &= \sum_i^{inclined} \frac{l_i}{EA} T_i^0 T_i^0 (P = 1) = \frac{lP}{E_s A} ((4N - 2)\sqrt{2}\sqrt{2}) \\
&= \frac{lP}{E_s A} (8N - 4).
\end{aligned} \tag{47}$$

The virtual work expression for straight bars is calculated from Figure 13 and Table 5 and then multiplied by 4 to consider all sides. For the straight bars, the side that is in compression the force decreases by $2P$ after each node, and for the side in tension the force increases by $2P$ for every node. Due to symmetry, the forces are equal for other sides, except for the sign changes. Unit cell where $N = 1$ contains 8 straight struts that are $\sqrt{2}l/4$ long and each have absolute force $P/2$. Increasing N incrementally adds one inclined bar length l to the structure shown in Figure 13, which results in an increase of $\sqrt{2}l/2$ in length on both sides to the straight bars. Adding one inclined bar creates one additional joint increasing the absolute bar forces on one of the sides. Using this information, the contribution to virtual work is given by:

$$W^{straight} = 8 * \frac{\sqrt{2}l}{4E_s A} * \frac{P}{2} * \frac{1}{2} + \sum_{k=1}^{N-1} \left(4 \frac{\sqrt{2}lP}{2E_s A} \left(2k^2 + \frac{1}{2} \right) \right). \quad (48)$$

After simplifying the equation, the contribution to virtual work becomes:

$$W^{straight} = \frac{2\sqrt{2}lP}{E_s A} \left(\frac{2N^3}{3} - N^2 + \frac{5N}{6} - \frac{1}{4} \right). \quad (49)$$

The last part of the calculations is the contribution of the center of the unit cell. To calculate the bar forces in the center, the force applied by the surrounding bars must be solved first and these are labelled in Figure 14. Due to symmetry, the forces need to be solved for one corner of the center only.

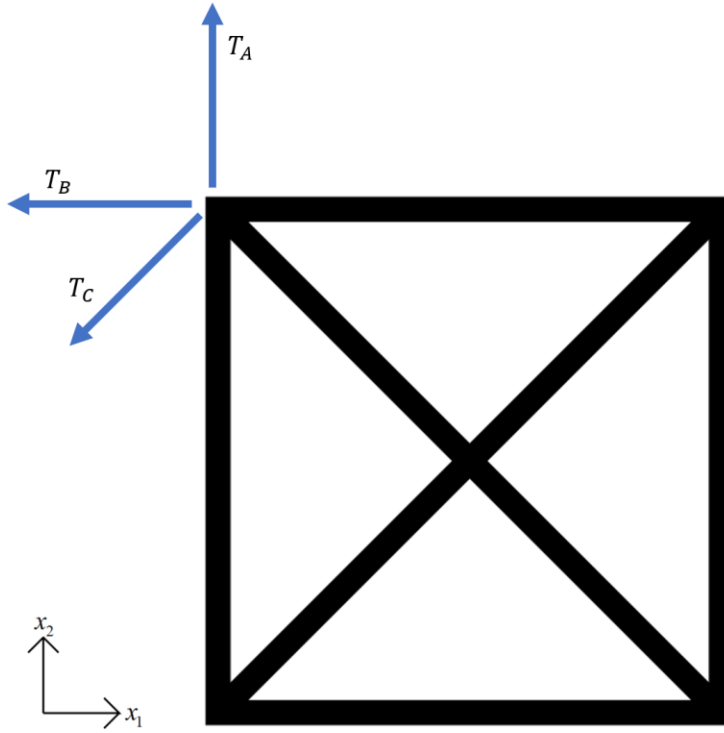


Figure 14: Forces applied to the unit cell center.

From Equation (43), we know that $T_A = P/2$ when $N = 1$. For a unit cell where $N = 2$ an additional joint is added on the side in tension. This increases the bar force by $2P$, but the outermost inclined bar changes direction resulting in a bar force decrease of $1P$, because the outermost straight bars are now in compression. The value of T_A is thus equal to $3P/2$. As the pattern is repeating the equation for T_A is

$$T_A = \left(N - \frac{1}{2}\right)P. \quad (50)$$

The side corresponding to T_B is also in tension except for a unit cell where $N = 1$. Equation (43) and Figure 11 show that the bar force is $T_B = -P/2$ for $N = 1$. Due to symmetry the pattern is the same as for bar force T_A except for the starting value resulting in the following expression:

$$T_B = \left(N - \frac{3}{2}\right)P. \quad (51)$$

Finally, calculations in Table 5 show that the absolute value of bar forces in the inclined bars is constant. Adding inclined bars does not change the sign of the force of the previous inclined bars due to sign change in the outermost inclined bar so T_C can be taken from Figure 11 and Equation (44) and is:

$$T_C = \sqrt{2}P. \quad (52)$$

With the forces applied to the corner of the center known, the bar forces in the center can now be solved for by examining the joint in the corner. Based on the symmetry of the unit cell and loading, it is assumed that the straight bars and inclined bars in the center have constant absolute forces T_D and T_E , respectively. For the joint to be in equilibrium one side of the center must be in compression and the other side in tension. Figure 15 shows the forces applied to the joint.

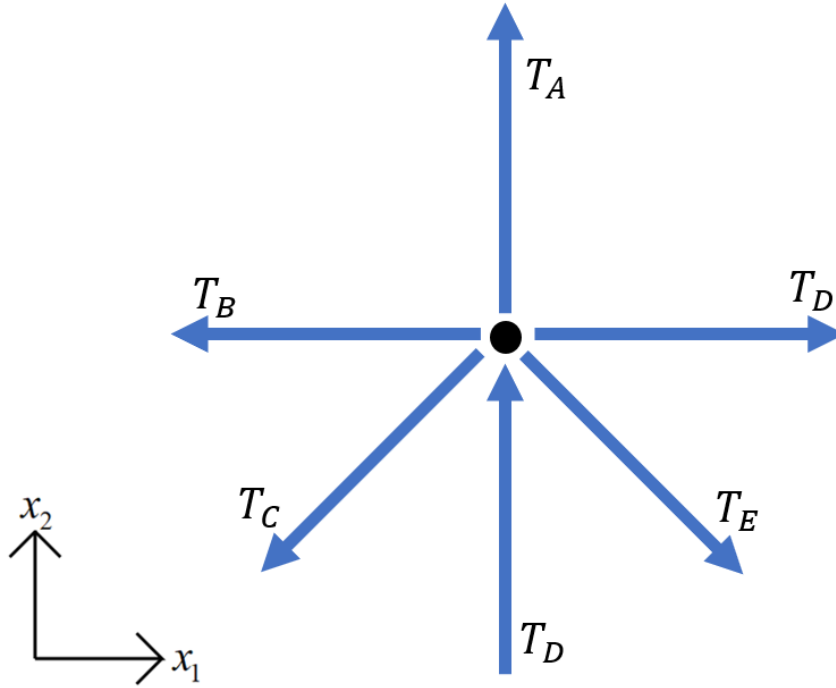


Figure 15: Forces in the corner joint.

The equilibrium equations in x_1 and x_2 -directions are

$$T_D - \left(N - \frac{3}{2}\right)P - P + \frac{\sqrt{2}}{2}T_E = 0 \quad (53)$$

and

$$T_D + \left(N - \frac{1}{2}\right)P - P - \frac{\sqrt{2}}{2}T_E = 0. \quad (54)$$

Solving Equations (53) and (54) gives

$$T_D = \frac{P}{2} \quad (55)$$

and

$$T_E = \sqrt{2}(N - 1)P. \quad (56)$$

The center contains two bars of length l that have an absolute bar force of T_E and four bars of length $\sqrt{2}l/2$ that have an absolute bar force of T_D . This gives the final virtual work expression

$$W^{center} = \frac{lP}{E_s A} \left(2 \left(\sqrt{2}(N-1) \right)^2 + \frac{\sqrt{2}}{2} \right). \quad (57)$$

Substituting virtual work expressions (47), (49), and (57) to (46) results in the combined displacement in x_1 and x_2 -directions

$$u_1 + u_2 = \frac{lPN}{3E_s A} (4\sqrt{2}N^2 - 6N(\sqrt{2} - 2) + 5\sqrt{2}). \quad (58)$$

For a pure shear, the shear strain for small rotations is given by a sum of the two displacements divided by the unit cell length:

$$\varepsilon_{12} = \frac{u_1 + u_2}{\sqrt{2}Nl}. \quad (59)$$

The shear stress is given by dividing the applied force by the side of the unit cell length and the out-of-plane thickness, giving:

$$\tau_{12} = \frac{P}{\sqrt{2}Nlt_o}. \quad (60)$$

Substituting Equations (59) and (60) to Equation (40) and dividing by the Young's modulus of the solid returns the relative shear modulus. This can be expressed as a function of relative density using Equation (22):

$$\frac{G_{12}}{E_s} = \frac{3(2 - \sqrt{2})}{4(4N^2 + 6N(\sqrt{2} - 1) + 5)} \bar{\rho} = \frac{0.1098}{N^2 + 0.6213N + 1.25} \bar{\rho}. \quad (61)$$

This equation shows that the shear modulus decreases exponentially towards zero as N is increased.

3.2 Finite element modelling

Periodic boundary conditions are used to predict the in-plane elastic properties of the lattice material in the finite element package Abaqus. Wu et al.

(2014, p. 707) describe periodic boundary conditions as a “set of boundary conditions that can be used to simulate a large system (i.e. bulk material) simply by modelling a finite Representative Volume Element (RVE)”. In the case of lattices, the Representative Volume Element is the unit cell, and this can be used to model the response of the lattice material using periodic boundary conditions. This can be beneficial as simulating a large lattice structure requires more computational resources than a single unit cell.

Periodic boundary conditions can be applied in Abaqus by constraining the nodes at the boundary. Tankasala et al. (2017) have presented the following equations for constraining the boundary nodes

$$\Delta u_i = \varepsilon_{ij} \Delta X_j \quad (62)$$

and

$$\Delta \theta = 0, \quad (63)$$

where X is a vector connecting two corresponding points. Equations (62) and (63) apply to corresponding nodes that are opposite of each other on the boundary of the unit cell. Figure 16 shows the node pairs of the unit cell where each number represents a pair. Each node pair will have to satisfy equations (62) and (63). In this two-dimensional case equation (62) must be applied to x_1 and x_2 directions.

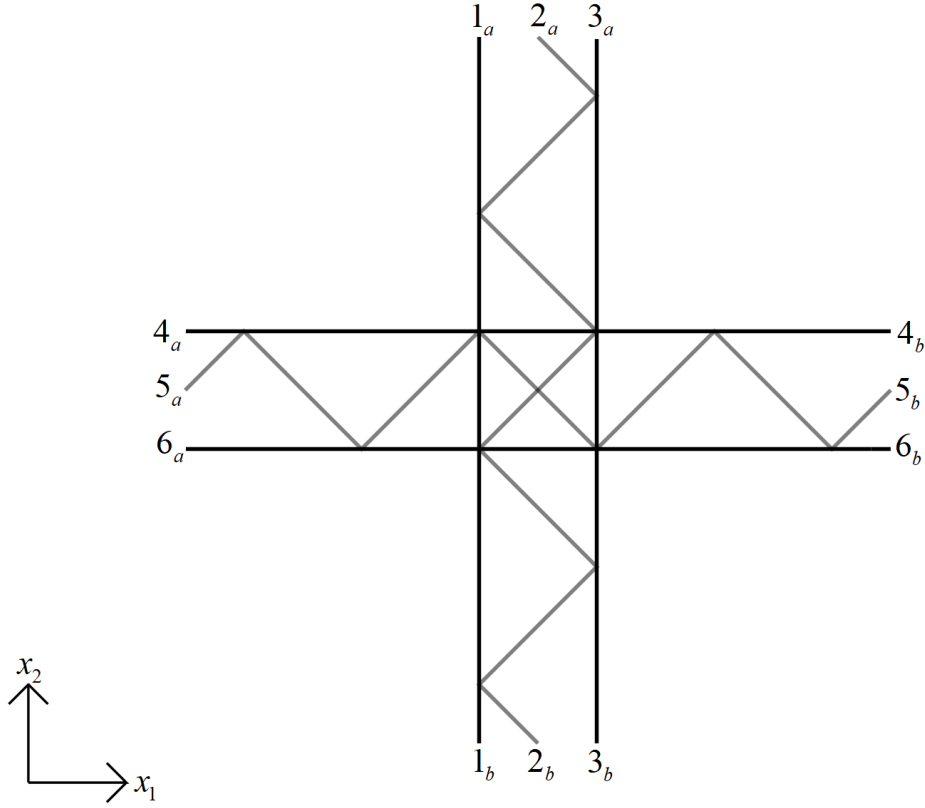


Figure 16: Node pairs of the unit cell.

3.2.1 Young's modulus

The Young's modulus is determined by applying an upward displacement to node 1_a and pinning the pair of this node 1_b . This results in a strain component:

$$\varepsilon_{22} = \frac{u_2^{1a}}{h}. \quad (64)$$

Node pairs 2 and 3 also need to respect Equation (62) and therefore, have the same strain ε_{22} as node pair 1. This gives the following constraint:

$$u_2^{1a} - u_2^{1b} = u_2^{2a} - u_2^{2b} = u_2^{3a} - u_2^{3b}. \quad (65)$$

Next, Equation (62) can be applied to the top nodes along the x_1 direction. Since the distance $\Delta X_1 = 0$, the constraints are:

$$\varepsilon_{11} \Delta X_1 = u_1^{ia} - u_1^{ib} = 0 \text{ for } i = 1, 2, 3. \quad (66)$$

The nodes 4, 5 and 6 on the side of the unit cell can be constrained starting from direction x_1 . ΔX_1 is non-zero for these node pairs and ε_{11} is also non-zero as the lattice can expand in x_1 direction. Node pair 4 can be left unconstrained, but to satisfy Equation (62) node pairs 4, 5 and 6 must have the same strain ε_{11} , which gives:

$$u_1^{4a} - u_1^{4b} = u_1^{5a} - u_1^{5b} = u_1^{6a} - u_1^{6b}. \quad (67)$$

For direction x_2 , the distance $\Delta X_2 = 0$ and the constraints become:

$$\varepsilon_{22}\Delta X_2 = u_2^{ia} - u_2^{ib} = 0 \text{ for } i = 4, 5, 6. \quad (68)$$

Finally, Equation (63) can be satisfied by setting rotation of each node in a pair equal, and this returns:

$$\theta^{ia} - \theta^{ib} = 0 \text{ for } i = 1, 2, 3, 4, 5, 6. \quad (69)$$

With all the constraints applied, the simulation can now be run. The simulation returns the reaction force P along the x_2 direction at node 1_a , and it can be used to calculate the stress:

$$\sigma_{22} = \frac{P}{wt_o}. \quad (70)$$

With known values of ε_{22} and σ_{22} they can be substituted in equation (23) to calculate the Young's modulus of the lattice material.

3.2.2 Poisson's Ratio

The Poisson's ratio is defined by dividing the transverse strain by the axial strain, as shown in Equation (35). The Poisson's ratio can be calculated from the simulation detailed in the previous section, where the strain component ε_{22} is known and the strain component perpendicular to the loading direction, ε_{11} , is calculated from the displacement of the nodes on each side as:

$$\varepsilon_{11} = \frac{u_1^{ib} - u_1^{ia}}{w} \text{ for } i = 4, 5, 6. \quad (71)$$

Any of the node pairs on the side of the unit cell can be selected as enforcing Equation (62) implies that ε_{11} is the same for all node pairs.

3.2.3 Shear modulus

For the shear modulus, new boundary conditions must be created. Expanding Equation (62) for a two-dimensional model gives:

$$\Delta u_1 = \varepsilon_{11}\Delta X_1 + \varepsilon_{12}\Delta X_2 \quad (72)$$

and

$$\Delta u_2 = \varepsilon_{21}\Delta X_1 + \varepsilon_{22}\Delta X_2. \quad (73)$$

Applying simple shear, results in $\varepsilon_{11} = \varepsilon_{22} = \varepsilon_{21} = 0$. A horizontal displacement is applied to node 1_a and node 1_b is pinned to induce a shear strain:

$$\varepsilon_{12} = \frac{u_1^{1a}}{h}. \quad (74)$$

Since $\varepsilon_{22} = \varepsilon_{21} = 0$, Equation (73) is equal to zero for all node pairs, which returns:

$$u_2^{ia} - u_2^{ib} = 0 \text{ for } i = 1, 2, 3, 4, 5, 6. \quad (75)$$

Node pairs on top and bottom must respect Equation (72) and this gives:

$$u_1^{1a} - u_1^{1b} = u_1^{2a} - u_1^{2b} = u_1^{3a} - u_1^{3b}. \quad (76)$$

For side nodes, $\Delta X_2 = 0$ and Equation (72) results in:

$$u_1^{ia} - u_1^{ib} = 0 \text{ for } i = 4, 5, 6. \quad (77)$$

Equation (63) can be satisfied by constraining the rotation of boundary nodes as presented in Equation (69). The reaction force P from node 1_a can be extracted from the simulation and used to calculate the shear stress using Equation (60). Finally, Equations (74) and (60) can be substituted in Equation (40) to calculate the shear modulus.

3.3 Results

The finite element simulations are performed using the finite element package Abaqus. All the simulations performed are linear as the material of the strut walls is elastic, and nonlinear effects of large deformations are ignored as rotations and deformations are assumed to be small. The simulation is set to be 2D planar and Timoshenko beam elements that allow transverse shear deformation are used (B21 in Abaqus). The cross-section of the beams is rectangular. The relative density range studied is 0.0005 to 0.095 except for unit

cells with high value of N . This is due to Equation (22) showing that relative density decreases when the number of triangular elements N is increased. This means that to achieve similar relative densities a high value of t/l is required. As Timoshenko beam elements provide adequate accuracy for cross-sectional dimensions up to $1/8$ of axial distance the maximum value of t/l is set to approximately 0.1 in the simulations (Abaqus documentation). It should also be noted that lattices that have a high value of stockiness contain high amount of overlapping eventually resulting in the entire lattice structure disappearing.

The simulation in tension, used to determine Young's modulus and Poisson's ratio, was not sensitive to mesh size. A mesh size corresponding to 10 elements per strut of length l produced approximately the same Young's modulus and Poisson's ratio than one with 20 elements per strut (less than 1% difference). The simulation used to determine shear modulus is also insensitive to mesh size and the difference in shear modulus was less than 1% when comparing 10 beam elements in each strut to 20 beam elements in each strut.

3.3.1 Young's modulus

The Young's modulus is predicted using a unit cell with periodic boundary conditions that can be seen in section 3.2.1. The displacement u_2 applied to node 1_a corresponds to a strain component of $\varepsilon_{22} = 0.001$ according to Equation (64). Figure 17 shows the axial stresses of the beams for a $N = 3$ unit cell where $\bar{\rho} = 0.095$. The load is mostly carried by the struts that are parallel to the loading direction and the center of the unit cell as assumed in the analytical prediction, see section 3.1.1.

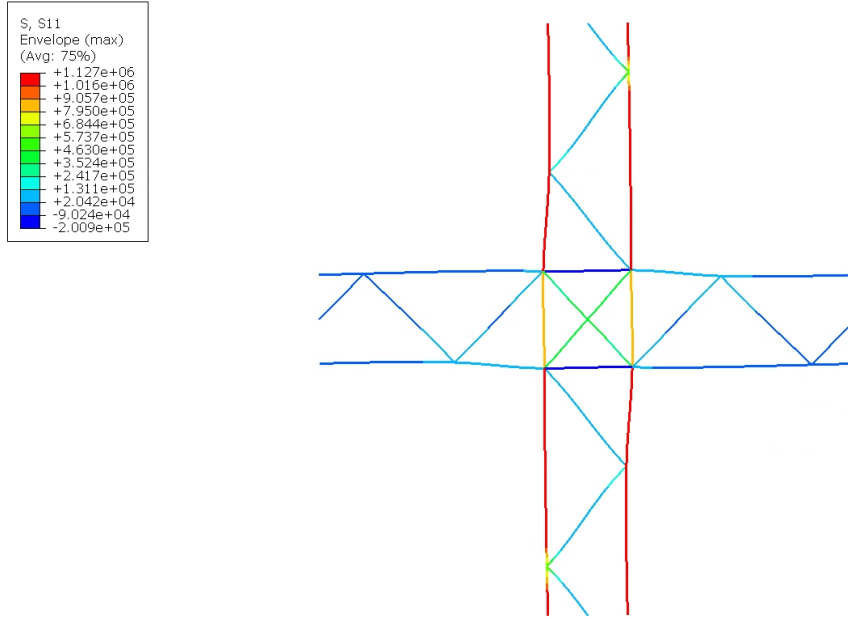


Figure 17: Deformed unit cell in tension where $N = 3$ and $\bar{\rho} = 0.095$.

Due to the linearity of the simulation, Equation (23) can be used to calculate the Young's modulus of the lattice material. The relative density $\bar{\rho}$ and number of triangular elements N is varied in the simulations to find coefficient B and exponent b of the scaling law presented in Equation (5). The length of the triangular element struts l is kept fixed as changing l scales the unit cell without making the unit cell more slender or thicker. This contrasts with changing N that changes the ratio of length scales of the triangular and square lattices. Due to this l/t can be treated as a single variable that is used to change the relative density.

First l is set to 10 mm and unit cells with different number of triangular elements N are simulated using a range of relative densities. Figure 18 contains only three of the values of N simulated for clarity as the difference between results is small, but measurable. The difference between the Young's modulus of a unit cell containing a single triangular element and one containing 100 triangular elements is approximately 10%.

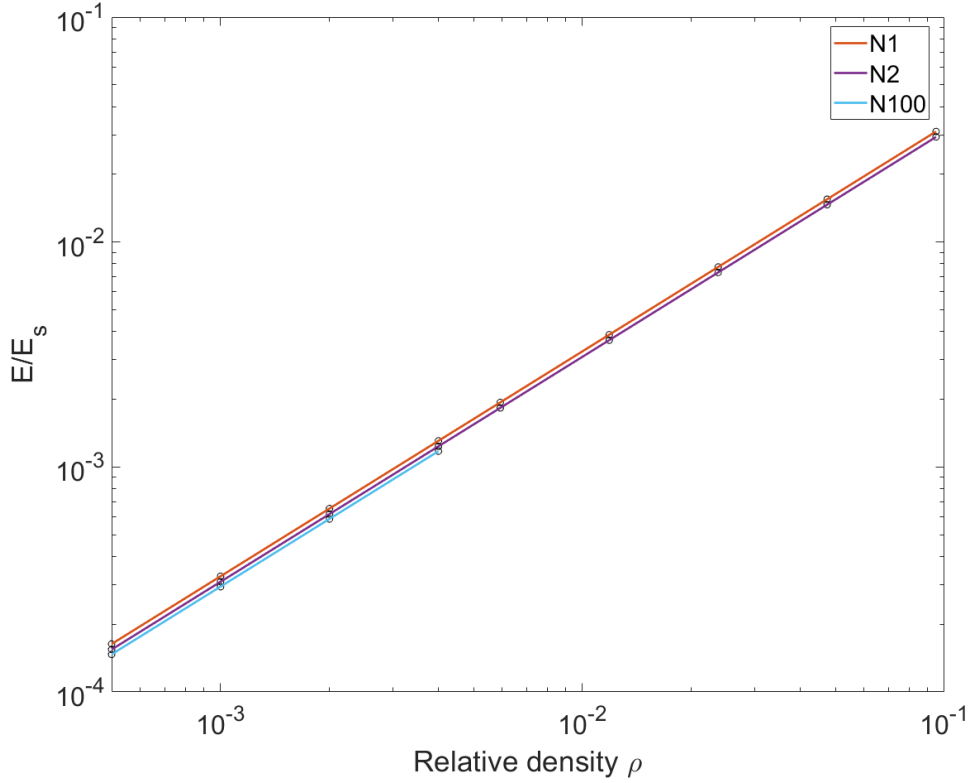


Figure 18 Relative Young's modulus.

Table 6 shows the equations for the relative Young's modulus for all values of N simulated. Table 6 also shows that the Young's modulus is a linear function of relative density meaning that the lattice is stretching-dominated. Compared to triangular and Kagome lattices that have coefficients $B = 1/3$ and $b = 1$ the stiffness of hierarchical square lattice is very similar. Compared to nonhierarchical square the Young's modulus is approximately 35% lower, see Table 1.

Table 6: Equations for the relative Young's modulus.

N	E/E_s
1	$0.3269\bar{\rho}^{1.000}$
2	$0.3094\bar{\rho}^{1.000}$
3	$0.3043\bar{\rho}^{1.001}$
4	$0.3021\bar{\rho}^{1.001}$
5	$0.3011\bar{\rho}^{1.001}$
6	$0.3008\bar{\rho}^{1.002}$
100	$0.2947\bar{\rho}^{1.001}$

The simulated values are in good agreement with the analytical formula derived in section 3.1.2 as shown in Figure 19. For high values of N the

difference between FE simulation and analytical formula is the highest although still under 1%.

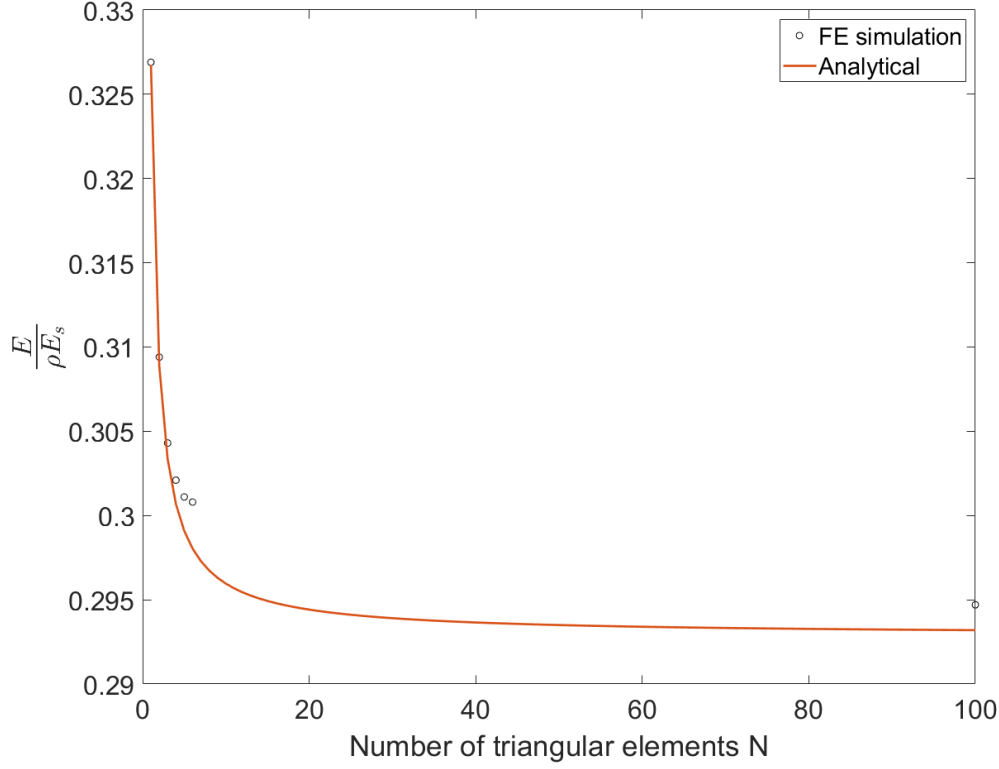


Figure 19: Comparison between FE and analytical results for the Young's modulus.

3.3.2 Poisson's ratio

The Poisson's ratio is calculated from the same simulation as the Young's modulus where the unit cell is in tension and strain is $\varepsilon_{22} = 0.001$. Poisson effect is not considered in the linear simulations resulting in the beam cross-section remaining constant (Abaqus documentation). This means that it is assumed that the Poisson's ratio of the lattice material is not dependent on the Poisson's ratio of the solid which is the case for many topologies. Exception to this is the Poisson's ratio of the square lattice that is a function of relative density and the Poisson's ratio of the solid. The unit cell of a square lattice consists of only two struts, and it could be assumed that the hierarchical square unit cell that consists of many struts would not be similarly dependant on the Poisson's ratio of the solid and that for low relative densities the Poisson's effect is negligible.

The simulations showed that the Poisson's ratio is nearly independent of the relative density which is expected due to the absence of Poisson's effect in the element's formulation. Only small changes in the Poisson's ratio

approximately 1% were measured when comparing the lowest and highest relative densities tested. Figure 20 shows the Poisson's ratio as a function of N . The FE simulation and analytical formula are in good agreement.

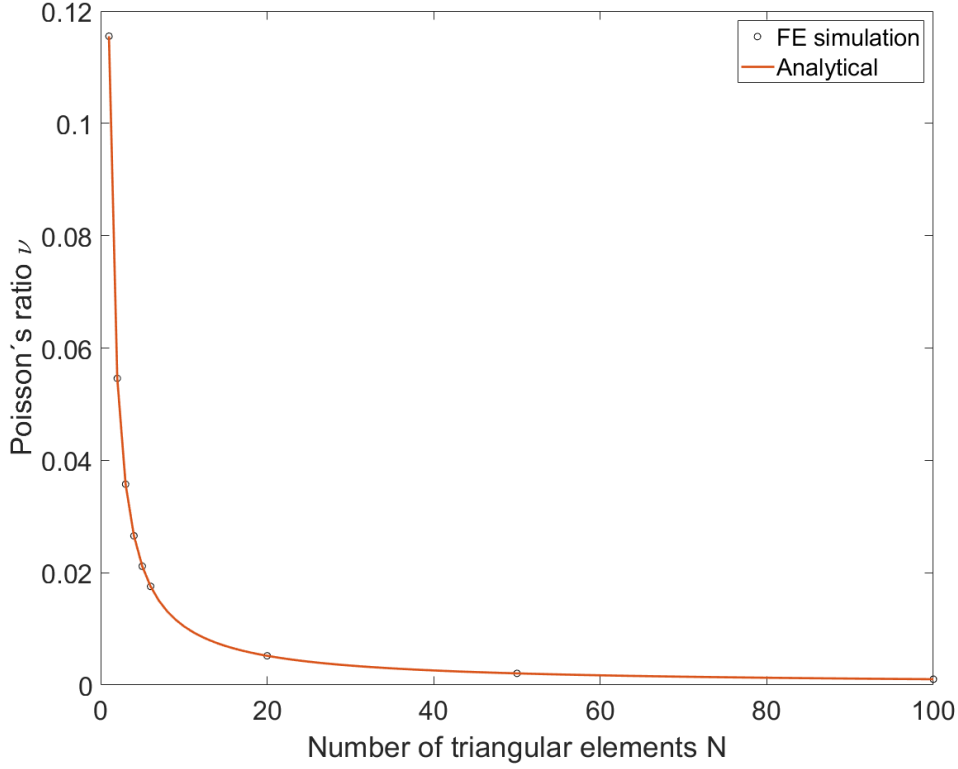


Figure 20: Comparison between FE and analytical results for the Poisson's ratio.

3.3.3 Shear modulus

The shear modulus is predicted using a unit cell with periodic boundary conditions described in section 3.2.3. The displacement u_1 applied to node 1_a corresponds to a strain component of $\varepsilon_{12} = 0.001$ according to Equation (74). Figure 21 shows the axial stresses on a unit cell with relative density of 0.095 and $N = 3$.

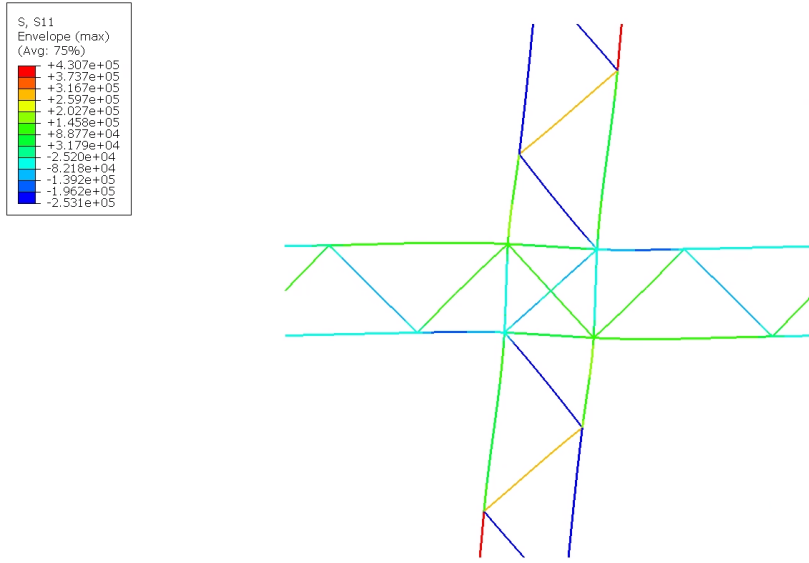


Figure 21: Deformed unit cell in shear where $N=3$ and $\bar{\rho} = 0.095$.

Figure 22 shows fitted curves of the datapoints and that the shear modulus of the lattice material is highly dependent on N ; increasing N considerably lowers the shear modulus. The shear modulus is approximately a linear function of relative density for each value of N . This indicates that the lattice material is stretching-dominated in shear. This is different from the square lattice, which is bending-dominated in shear (Wang and McDowell, 2004).

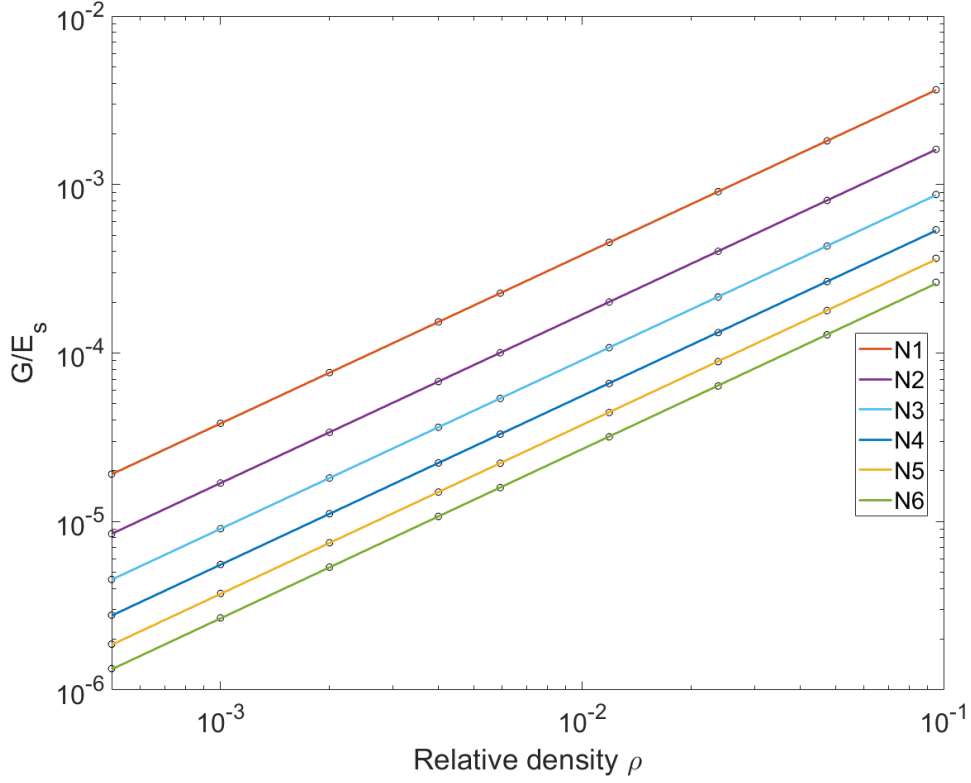


Figure 22: FE results of the shear modulus for $N = 1 - 6$.

Next, higher values of N are studied. Due to the previously mentioned restriction on stockiness the relative densities studied are limited to 0.0005-0.004. Figure 23 shows the shear modulus for high values of N . The shear modulus is orders of magnitude lower compared to unit cells with low value of N , but the shear modulus is still a linear function of relative density. The power-law expressions for each value of N can be seen in Table 7.

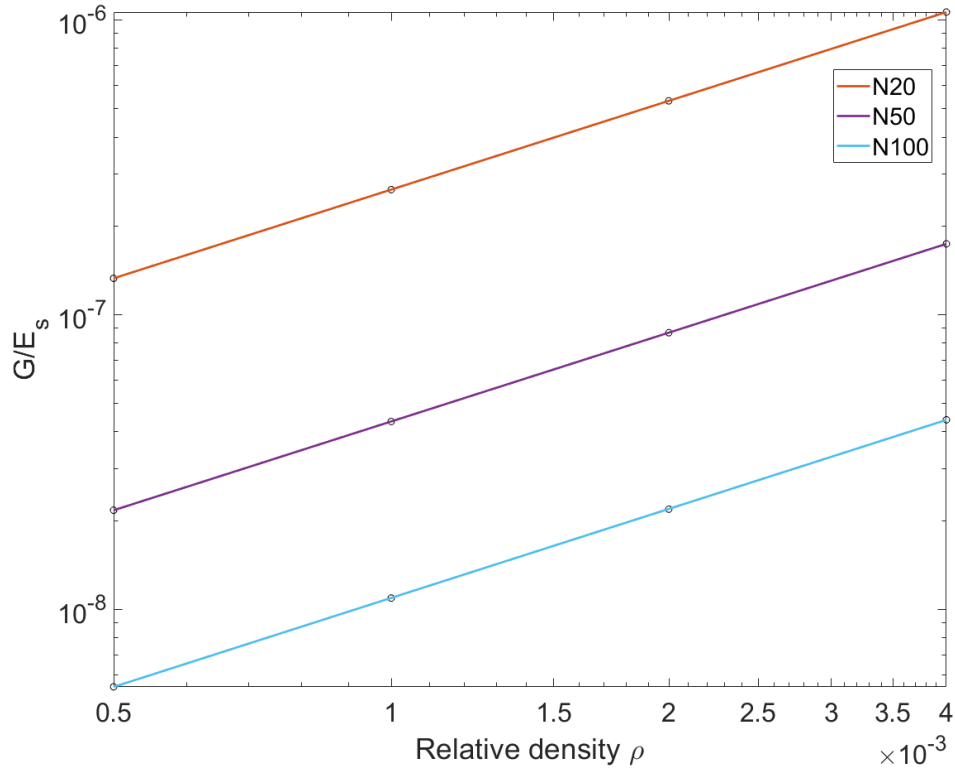


Figure 23: FE results of the shear modulus for $N=20, 50$, and 100 .

Table 7: relative shear modulus equations.

N	G/E_s
1	$0.03844\bar{\rho}^{1.001}$
2	$0.01703\bar{\rho}^{1.001}$
3	$0.009172\bar{\rho}^{1.002}$
4	$0.005658\bar{\rho}^{1.003}$
5	$0.003824\bar{\rho}^{1.004}$
6	$0.002756\bar{\rho}^{1.005}$
20	$0.0002659\bar{\rho}^{1.000}$
50	$0.00004365\bar{\rho}^{1.001}$
100	$0.00001117\bar{\rho}^{1.003}$

Figure 24 shows the coefficient of the shear modulus scaling law plotted as a function of N . The results from FE simulations and analytical formula are in good agreement.

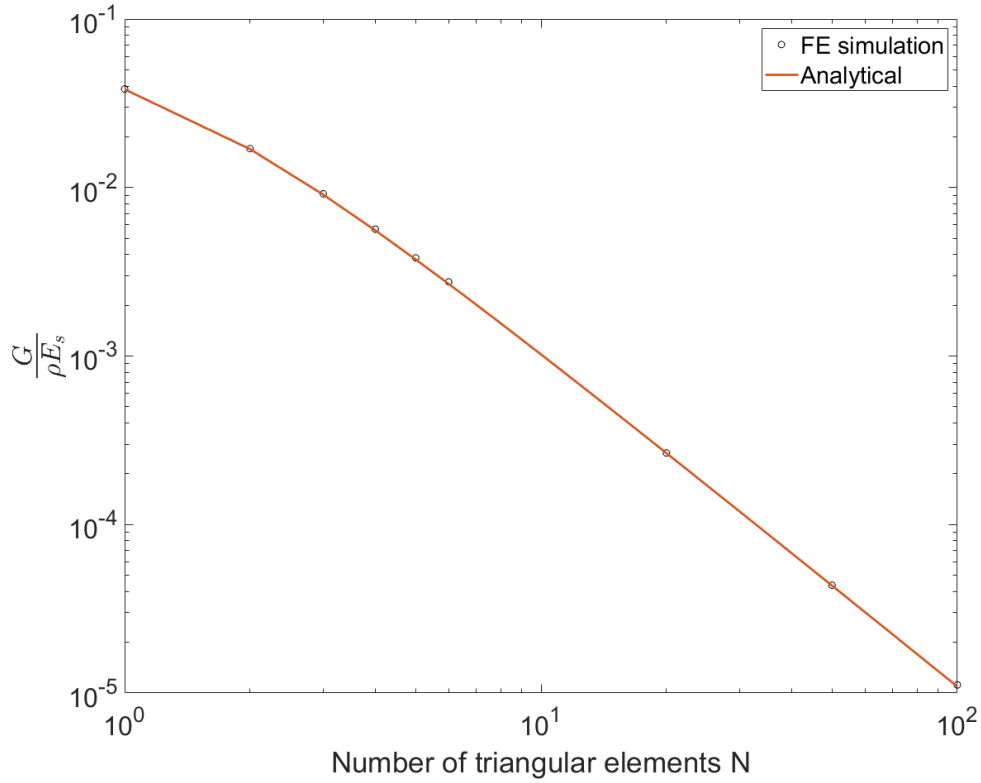


Figure 24 : Comparison between FE and analytical results for the shear modulus.

Finally, it can be concluded that the hierarchical square is not an isotropic material as it does not satisfy the following relationship:

$$G = \frac{E}{2(1 + \nu)}. \quad (78)$$

This is the same result as for the square topology, which deforms by beam stretching when loaded parallel to the struts and by beam bending when loaded at a 45° angle to cell struts resulting in a difference in stiffness (Wang and McDowell ,2004).

4 Fracture toughness

The fracture toughness of a hierarchical square lattice is predicted computationally using the finite element package Abaqus. The lattice material contains no defects, and the cell wall tensile strength is constant. First, the finite element modelling approach is given. The fracture toughness is predicted for mode I and mode II by first assuming that the lattice fails when any of the struts reach the tensile strength of the solid. Afterwards the fracture pattern is investigated to determine if the fracture toughness increases after the failure of the first strut. Finally, the fracture toughness of a hierarchical square lattice is compared to the nonhierarchical square lattice.

4.1 Finite element modelling

The fracture toughness is predicted using the boundary layer analysis introduced by Schmidt and Fleck (2001) based on continuum fracture mechanics. Boundary layer analysis is selected because of its computational efficiency and suitability for brittle-elastic materials. This method uses a finite lattice containing a crack that is implemented by removing beams. In this study, an edge crack is used. The removed beam elements form a continuous crack that is parallel to the x_1 -axis as shown in Figure 25. In the figure, only the crack tip is shown, and the actual lattice size is much larger.

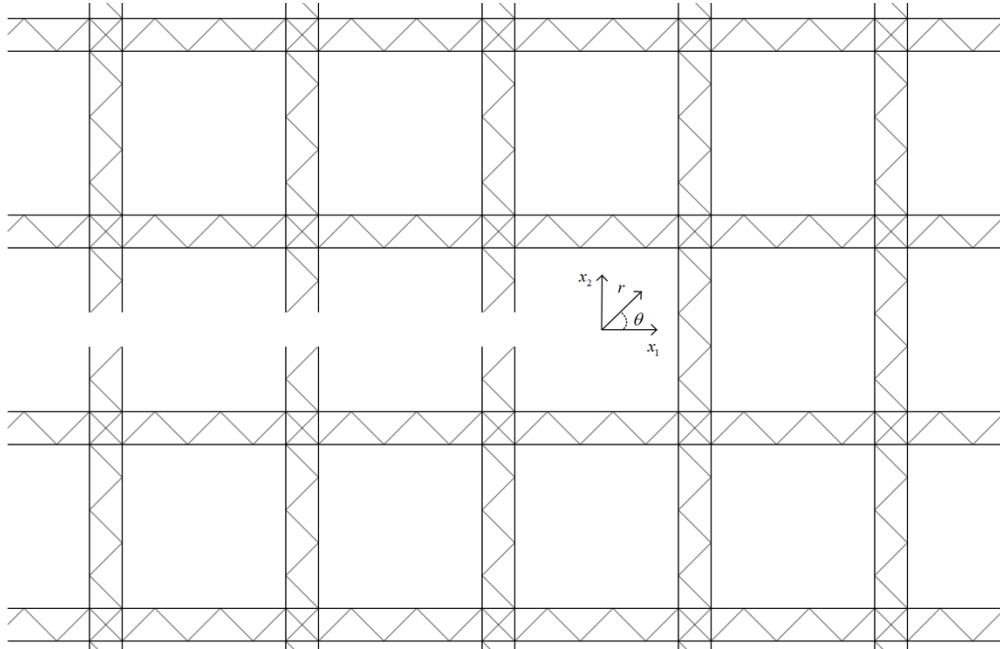


Figure 25: Crack tip and coordinate systems.

The lattice is assumed to be made from elastic-brittle beams, which fail when the tensile stress reaches the tensile strength of the solid. The crack is

subjected to a stress intensity K_{IC} or K_{IIC} by applying a displacement field to the outer boundary of the lattice according to the K-field. The K-field at the crack tip of an orthotropic elastic plate is given in Sih et al. (1965). The displacement field is calculated using the effective material properties of the lattice material and is applied to the outer boundary nodes using a Python script. This means that the displacements on the boundary of the finite lattice are assumed equal to a homogenous material possessing the material properties of the lattice.

After running the finite element simulation, the maximum tensile stress in any of the lattice struts can be located. Due to bending of the beams the maximum tensile stress is located on the outer most fiber of the beam. This means that the maximum tensile stress is obtained from section point 1 or 5 for a 2D beam (Abaqus documentation). The results are extrapolated to the nodes and each node is compared to find the maximum tensile stress. The fracture toughness corresponds to the value of stress intensity where the maximum tensile stress reaches the tensile strength σ_f of the solid material.

Furthermore, the axial stress of each beam element can be divided into bending induced stress and stretching induced stress. Stretching induced stress is constant on the top and bottom face of the element while the absolute value of bending induced stress is equal but opposite in sign on top and bottom faces. This gives the following equations

$$\sigma_n = \frac{\sigma_t + \sigma_b}{2} \quad (79)$$

and

$$\sigma_m = \pm \frac{\sigma_t - \sigma_b}{2}, \quad (80)$$

where σ_n is the stretching induced axial stress, σ_m is the bending induced axial stress, σ_t is the axial stress on the top face of the element, and σ_b is the axial stress on the bottom face of the element.

The fracture toughness of the lattice material is determined by enforcing plane strain conditions. Plane strain can be assumed for specimens with high out-of-plane thickness resulting in $\varepsilon_{33} = 0$. Enforcing plane strain condition requires modifying the material properties of the isotropic and elastic lattice beams according to equations

$$E_{ps} = \frac{E_s}{1 - \nu_s^2} \quad (81)$$

and

$$v_{ps} = \frac{v_s}{1 - v_s}. \quad (82)$$

The fracture toughness of thin specimens under plane-stress is higher compared to thick specimens subject to plane-strain. As the thickness of the specimen is increased the fracture toughness decreases until eventually plateauing when plane strain conditions are reached (Lynch et al., 2014). After the fracture toughness has reached a constant value, it can be considered as a material property as it is independent of the specimen thickness.

4.2 Results

The mode I and mode II fracture toughness was predicted for values of N ranging from 1 to 6. Unlike the Young's modulus of the solid the Poisson's ratio of the solid influences the nondimensional fracture toughness as seen in Equation (81). For all the fracture toughness simulations Poisson's ratio of the solid is set to 0.3. The Abaqus settings such as beam element type are kept the same as in in-plane elastic properties simulations.

4.2.1 Grid dependency

Before determining the fracture toughness of the lattice material, the sufficient number of unit cells and sufficient mesh size must be determined. First the number of unit cells is determined using a mesh size corresponding to 10 elements in each inclined strut of length l . Figure 26 shows the nondimensional mode I fracture toughness for a unit cell where $N = 6$ and the legend shows the number of unit cells on each side of the square lattice domain. Increasing the side length from 24 to 48 unit cells results in a 2% reduction in fracture toughness and increasing the side length from 48 to 98 unit cells decreases the fracture toughness by less than 1%. This shows that the mode I fracture toughness is not very sensitive to the number of unit cells. The lattice with side length of 48 unit cells is selected for mesh size analysis as the difference in fracture toughness compared to side length of 98 unit cells is negligible.

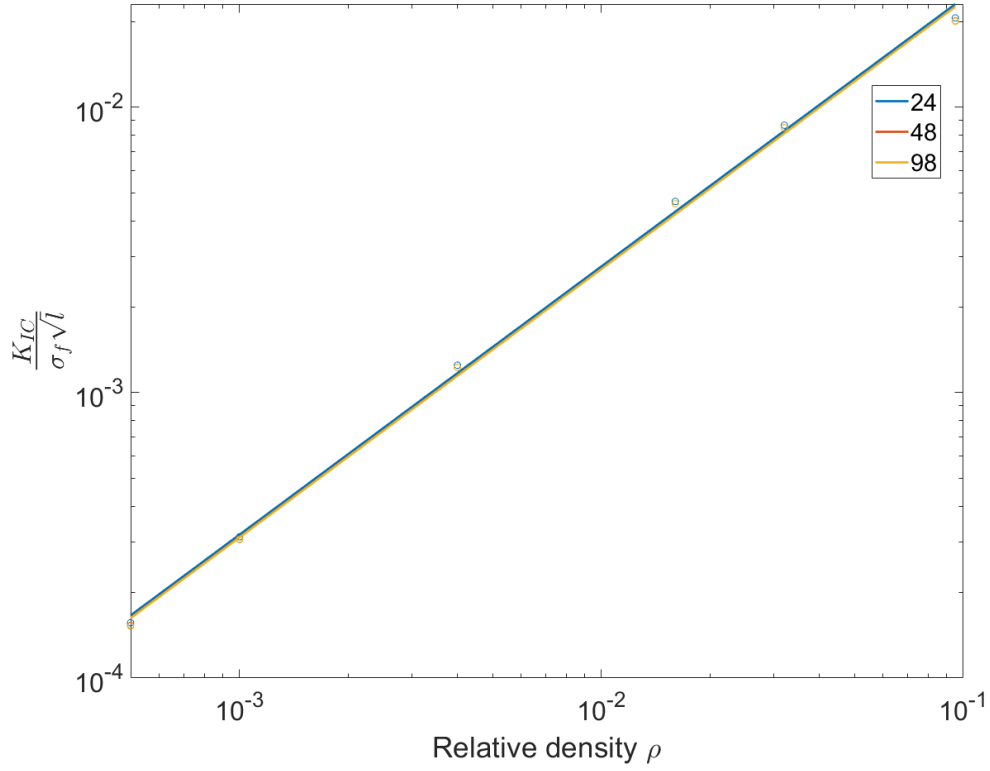


Figure 26: Effect of the number of unit cells on the mode I fracture toughness.

After determining the sufficient number of unit cells the number of beam elements in each inclined strut can be determined. Figure 27 shows the dependency of the nondimensional mode I fracture toughness on the number of elements in each strut for a unit cell where $N = 6$. Increasing the number of elements from 10 to 20 results in a 4% reduction in fracture toughness. Increasing the number of elements from 20 to 40 decreases the fracture toughness by 2%.

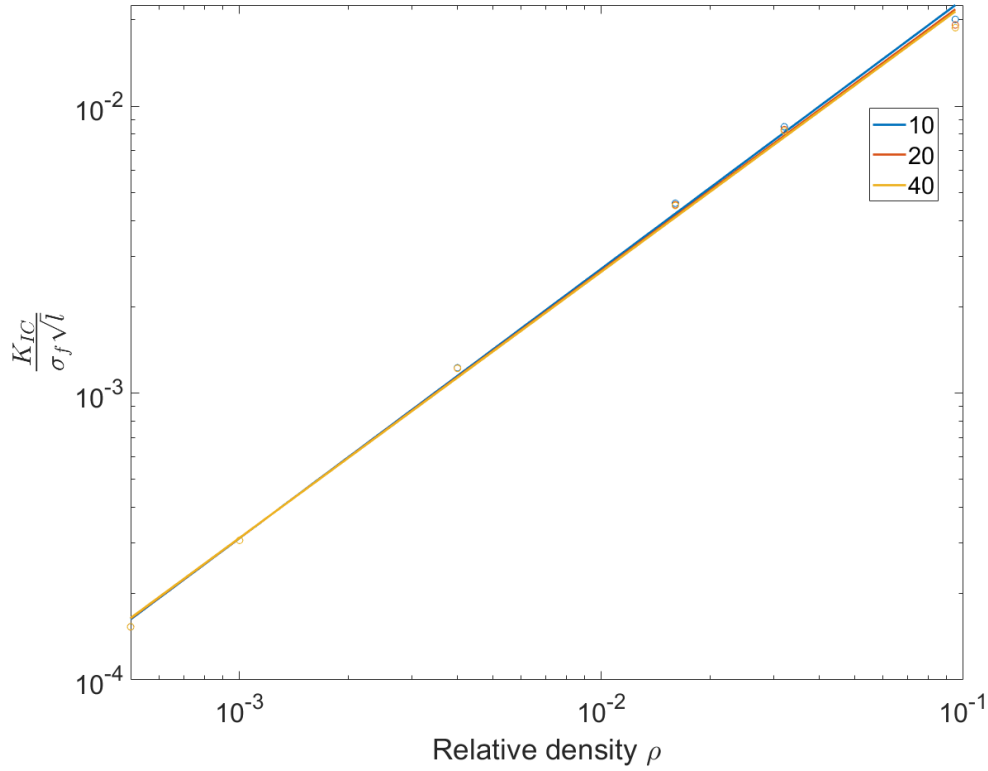


Figure 27: Effect of the mesh size (number of elements per strut) on the mode I fracture toughness.

The grid dependency analysis is repeated for the mode II fracture toughness. The nondimensional mode II fracture toughness for a unit cell where $N = 6$ is plotted in Figure 28 for three different lattice side lengths. Mode II is slightly more sensitive to the number of unit cells than mode I. Increasing the side length of the domain from 24 to 48 unit cells results in a 7% decrease in fracture toughness. Increasing side length from 48 to 98 unit cells decreases the fracture toughness by 3%. Therefore, a side length of 48 unit cells is selected for mesh analysis.

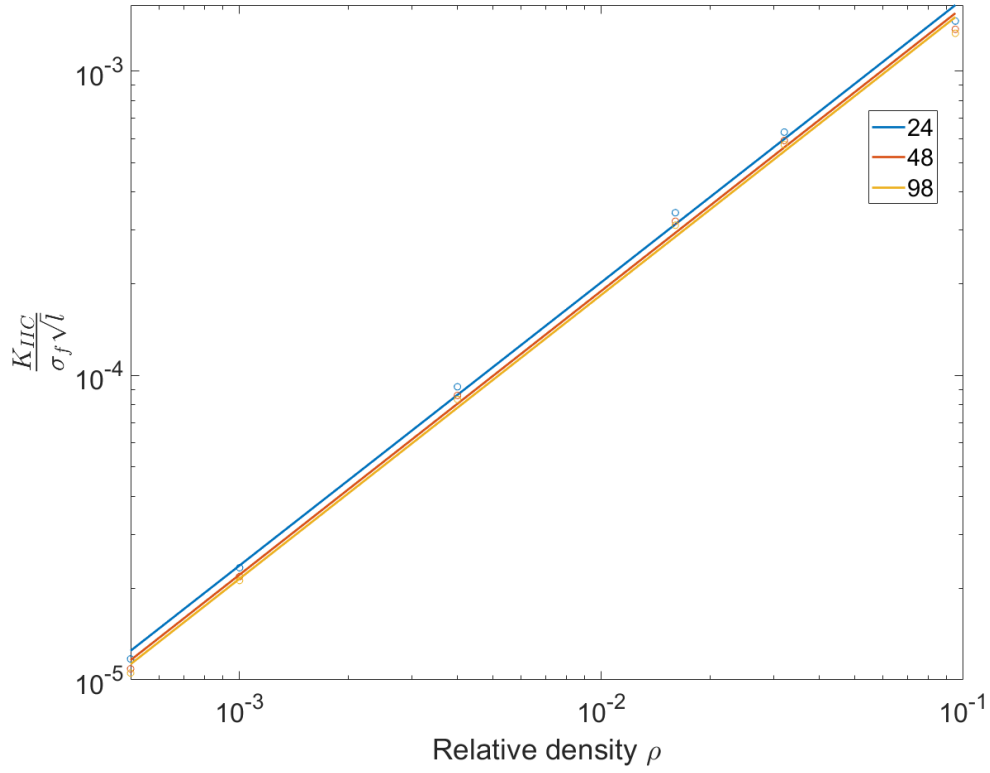


Figure 28: Effect of the number of unit cells on the mode II fracture toughness.

The nondimensional mode II fracture toughness dependency on the number of beam elements in each strut is shown in Figure 29. The results are similar to mode I as the nondimensional fracture toughness decreases up to 3% when number of elements in each strut is increased from 10 to 20. Increasing the number of elements in each strut from 20 to 40 results in a 2% reduction in fracture toughness.

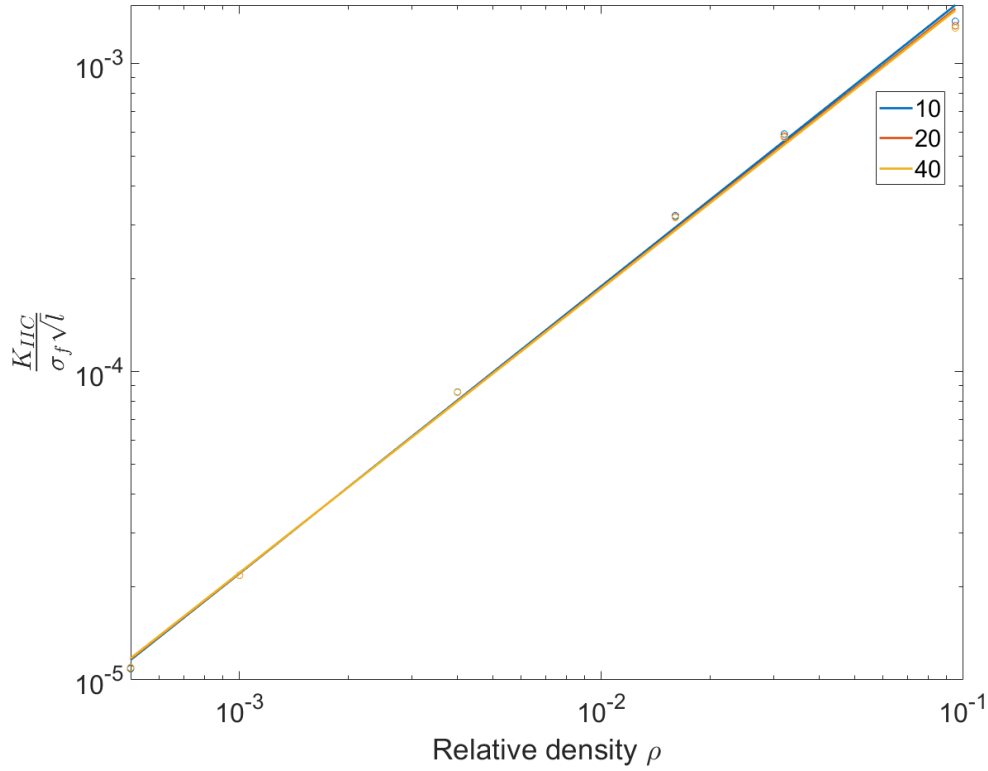


Figure 29: Effect of the mesh size on the mode II fracture toughness.

Next, it should be discussed if the grid dependency study is valid for all values of N simulated in the following sections. The lattice where $N = 6$ is the highest value of N for which the fracture toughness is determined in the following sections. Equation (22) shows that the stockiness of the lattice increases if N is increased. The grid dependency study shows that at higher stockiness the fracture toughness is more sensitive to the number of beam elements in each strut. This indicates that the number of elements in each strut that is sufficient for $N = 6$ is sufficient for lower values of N . Grid dependency studies on a unit cell where $N = 4$ and $N = 1$, which are not shown here, have confirmed this trend.

For mode I and mode II fracture toughness, the mesh size had 20 elements per strut and the lattice had a side length of 48 unit cells. These parameters gave an accurate fracture toughness at a reasonable computational time.

4.2.2 Mode I fracture toughness

Figure 30 shows the mode I nondimensional fracture toughness as a function of relative density. The fracture toughness seems to decrease, and the response becomes less linear as N increases. The fitted power equations can be seen in Table 8. The fitted curves closely match the datapoints for low relative densities, but the error increases for high relative densities.

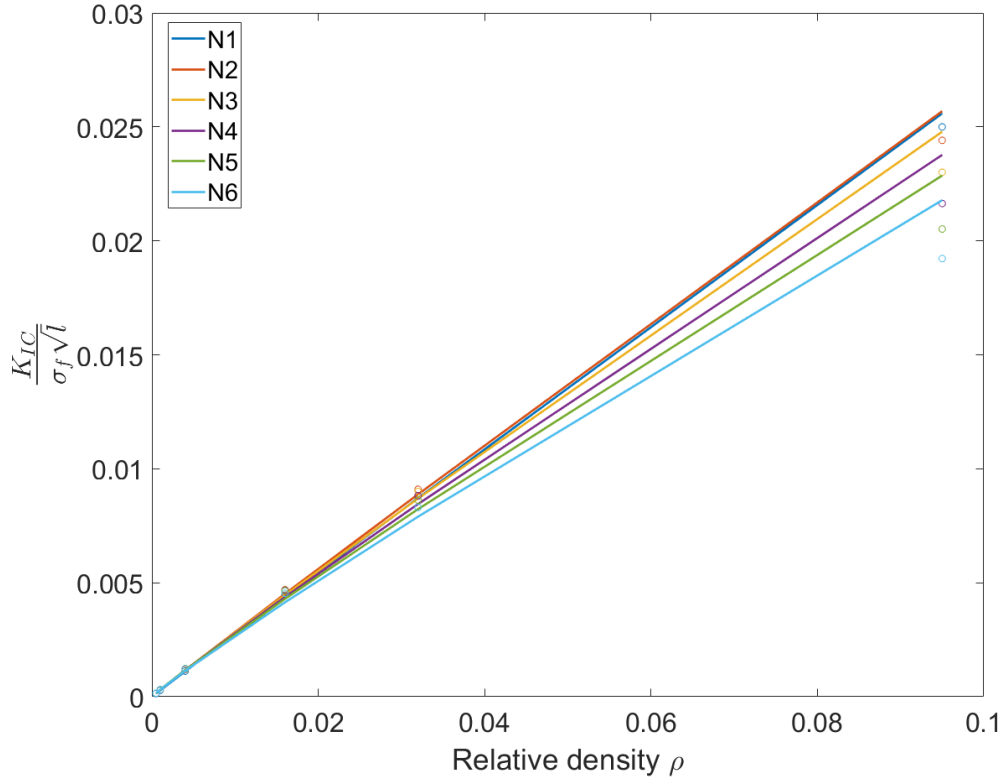


Figure 30: Mode I fracture toughness for different values of N .

Table 8: Mode I fracture toughness equations when relative density is varied from 0.005 to 0.095.

N	$\frac{K_{IC}}{\sigma_f \sqrt{l}}$
1	$0.2633\bar{\rho}^{0.9903}$
2	$0.2557\bar{\rho}^{0.9762}$
3	$0.2390\bar{\rho}^{0.9627}$
4	$0.2225\bar{\rho}^{0.9501}$
5	$0.2085\bar{\rho}^{0.939}$
6	$0.1954\bar{\rho}^{0.9320}$

To further examine the effect that N has on the fracture toughness the results are plotted as a function of stockiness in Figure 31. The datapoints correspond to the relative density displayed on the right side of the datapoints. The figure shows that the datapoints fall on an approximately straight line at low values of stockiness while at higher values the line resembles a downward slope. This indicates that at low values of stockiness the fracture toughness for different values of N is very similar. To show this the stockiness is limited

to a maximum of 0.02 corresponding to the stockiness value of $N = 1$ at $\bar{\rho} = 0.095$. Table 9 shows the equations for the fitted curves. Each value of N contains at least four datapoints.

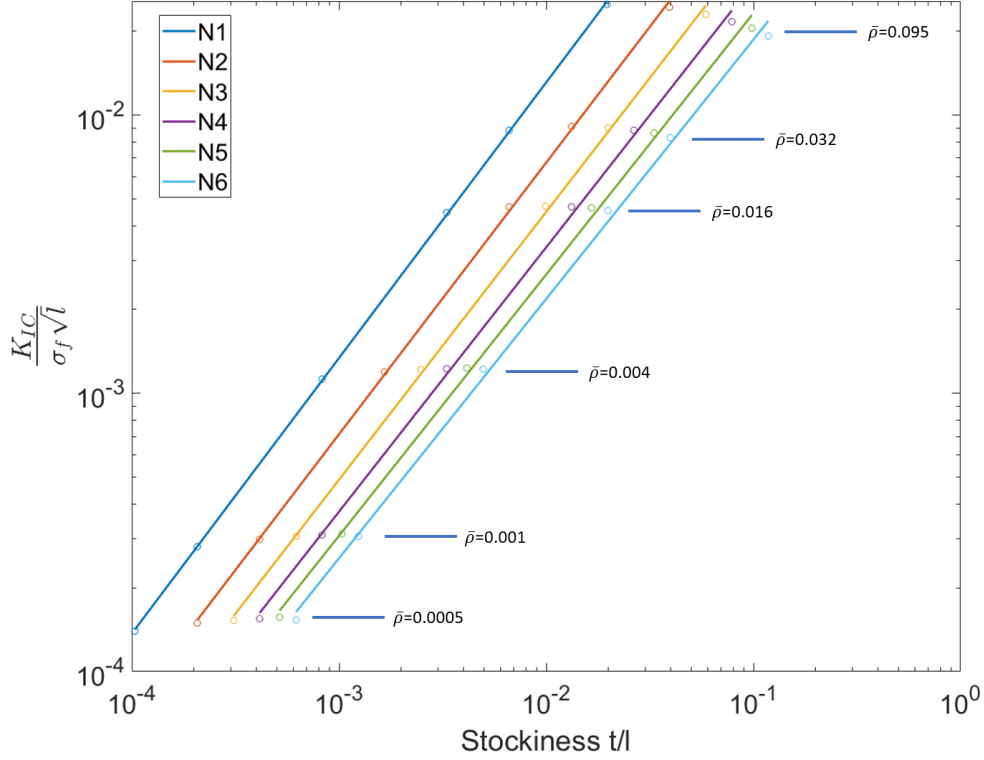


Figure 31: Mode I fracture toughness as function of stockiness.

Table 9: Mode I fracture toughness equations when stockiness is limited to a maximum of 0.02.

N	$\frac{K_{IC}}{\sigma_f \sqrt{l}}$
1	$0.2633\bar{\rho}^{0.9903}$
2	$0.2775\bar{\rho}^{0.9892}$
3	$0.2694\bar{\rho}^{0.9816}$
4	$0.2756\bar{\rho}^{0.9834}$
5	$0.2681\bar{\rho}^{0.9781}$
6	$0.2645\bar{\rho}^{0.9790}$

The above results indicate that the change in the lattice topology is not the reason for the change in fracture toughness. Instead, the value of N affects the stockiness of the lattice as seen in Equation (22). As relative density is increased the displacements in the lattice decrease and the beam thickness increases. The axial stresses induced by beam stretching are not affected by

the increasing thickness of the beam, but bending stresses increase as the thickness of the beam increases.

This was confirmed by examining the axial stresses on section points on the opposite surfaces of the beam at high and low relative densities. Examining the element experiencing the highest tensile stress in a $N = 6$ lattice shows that at $\bar{\rho} = 0.0005$ stretching induced axial stress is 418 times higher than the bending stress and at $\bar{\rho} = 0.095$ stretching induced axial stress is only 1.7 times higher than the bending stress. This means that the response of the lattice is becoming more bending-dominated at high stockiness.

4.2.3 Mode I fracture locations

The location where the maximum tensile stress is reached is investigated for different values of N in the specified relative density range. The fracture pattern is also investigated by removing the strut experiencing the highest tensile stress to see if failure of the strut results in macroscopic failure of the lattice. Figure 32 shows the deformed lattice where $N = 6$ and $\bar{\rho} = 0.095$ under mode I loading with exaggerated displacements. Vertical shear band and horizontal bending band can be seen originating from the crack tip. The crack profile is similar for all values of N tested.

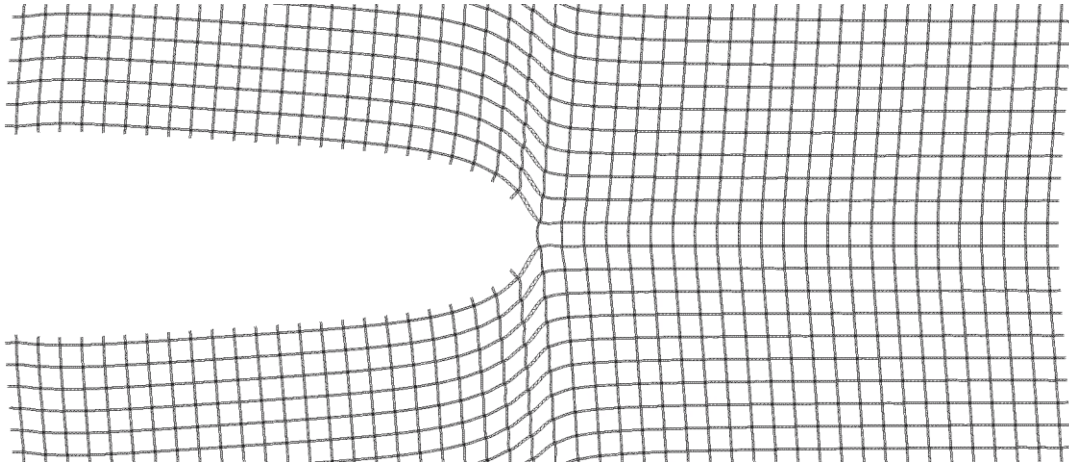


Figure 32: Deformed lattice under mode I loading when $N = 6$ and $\bar{\rho} = 0.095$.

Figure 33 shows the location of the first strut to fail on a unit cell where $N = 3$ for simplicity. For values of N up to 5 the failure occurs at one of the struts colored in red and for $N = 6$ the failure occurs at one of the struts colored in blue. Relative density affects the failure location so that the exact beam to fail can vary within the colored area.

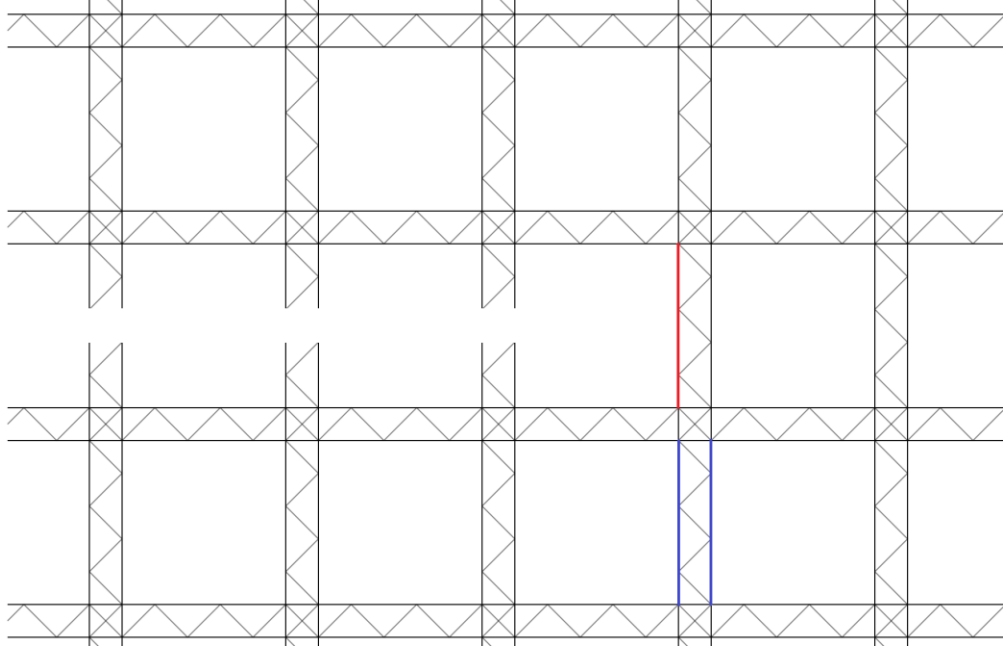


Figure 33: Mode I failure location.

Next, additional simulations were performed to assess if the first failure will lead to a macroscopic failure of the lattice. This is investigated by assuming that the strut attaining maximum axial stress fails and is therefore removed. After removing the failed strut, the simulation is performed again and the process repeated. The criterion for macroscopic failure of the lattice is that fracture toughness decreases as struts are broken. Figure 34 shows the fracture pattern for a lattice where $N = 1$, where A marks the first strut to fail and B marks the second strut to fail and so forth. Fracture toughness for each strut labeled in the figure is as follows

$$K_{IC}^A < K_{IC}^B > K_{IC}^C > K_{IC}^D. \quad (83)$$

Inequality (83) shows that after the first strut fails the fracture toughness increases and if strut B fails the lattice fails. The power-law expression for the fracture toughness corresponding to strut B failing is

$$\frac{K_{IC}}{\sigma_f \sqrt{l}} = 0.2966 \bar{\rho}^{0.9829}. \quad (84)$$

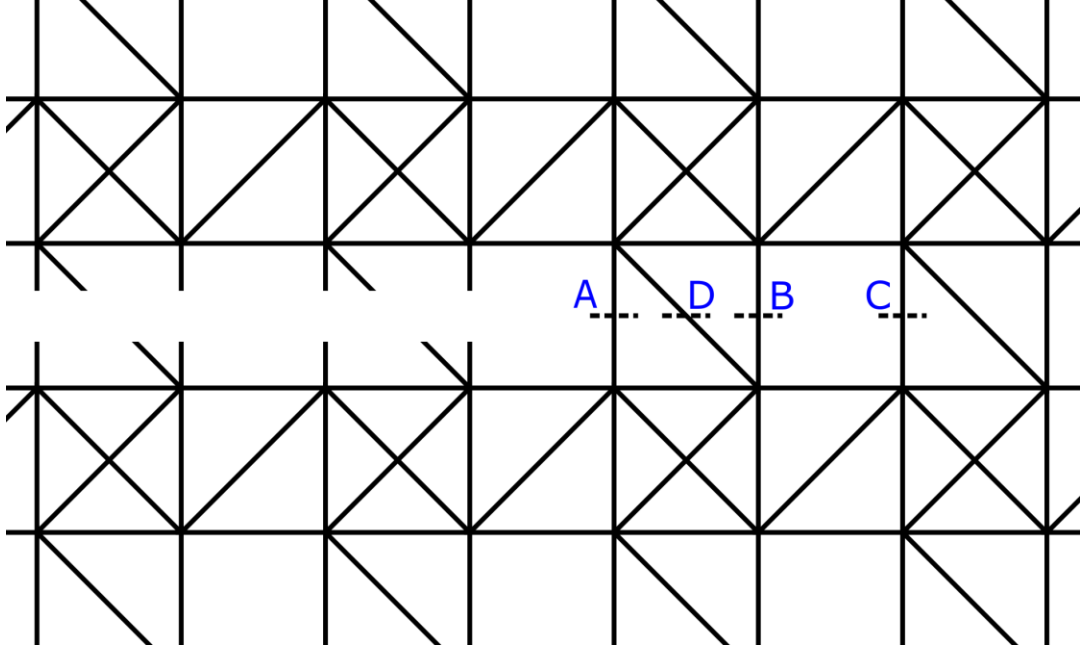


Figure 34: Mode I fracture pattern for $N = 1$ lattice.

For higher values of N , the fracture pattern depends on the relative density unlike for $N=1$. For values of N 2-5 the fracture pattern at high relative density is like the fracture pattern of $N = 1$. At low relative densities the pattern is shown in Figure 35, where it is illustrated using a lattice where $N = 3$ for simplicity. The struts ahead of the crack break in a way that leaves the inclined struts intact. The axial stress on the inclined struts is induced almost purely by bending of the strut resulting in low stresses at low relative densities due to the slenderness of the strut. The fracture toughness increases in the following manner

$$K_{IC}^D > K_{IC}^A > K_{IC}^C > K_{IC}^B. \quad (85)$$

This is because the crack tip is stationary resulting in a constant displacement field on the boundary. Although the inclined struts remain intact, the crack could be considered extended as the struts ahead of the crack tip have lost their stiffness almost entirely. The inclined struts could create bridging across the crack as the crack propagates affecting the fracture toughness, but this is beyond the scope of this thesis. It is concluded that failure of the first strut results in macroscopic failure of the lattice.

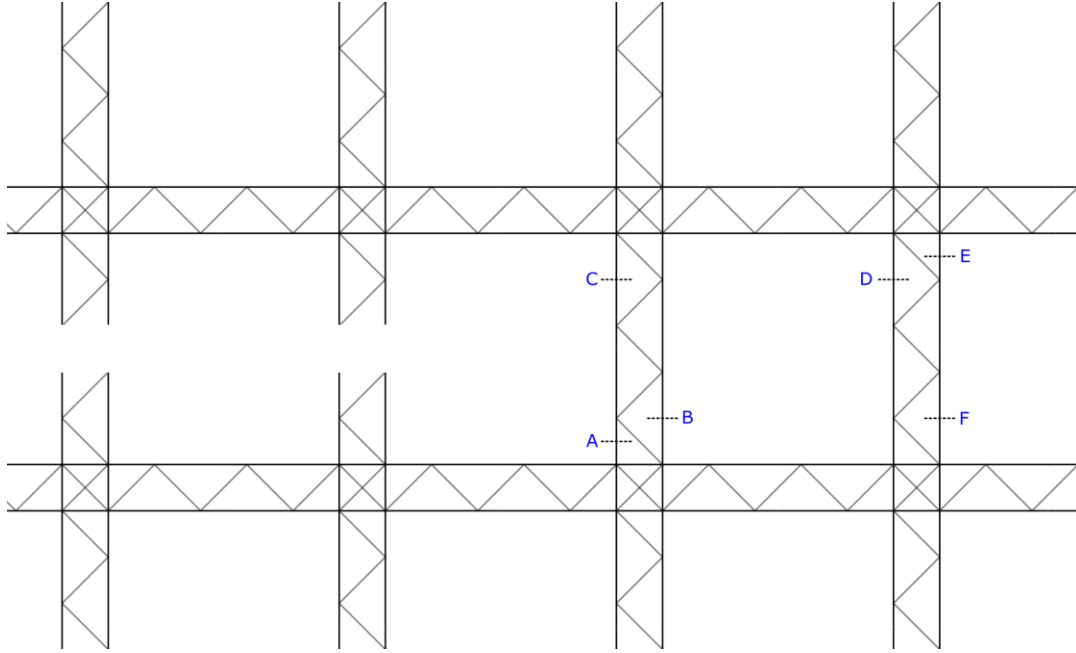


Figure 35: Mode I fracture pattern for N 2-5 lattices.

Finally, for a lattice where $N = 6$ the fracture pattern is like $N = 2 - 5$ with the exception that the fracture moves down as seen in Figure 33. For $N = 6$ it is also concluded that macroscopic failure occurs when the first strut breaks.

4.2.4 Mode II fracture toughness

Figure 36 shows the mode II nondimensional fracture toughness a function of relative density. The fracture toughness decreases as N is increased which is also the case for the shear modulus.

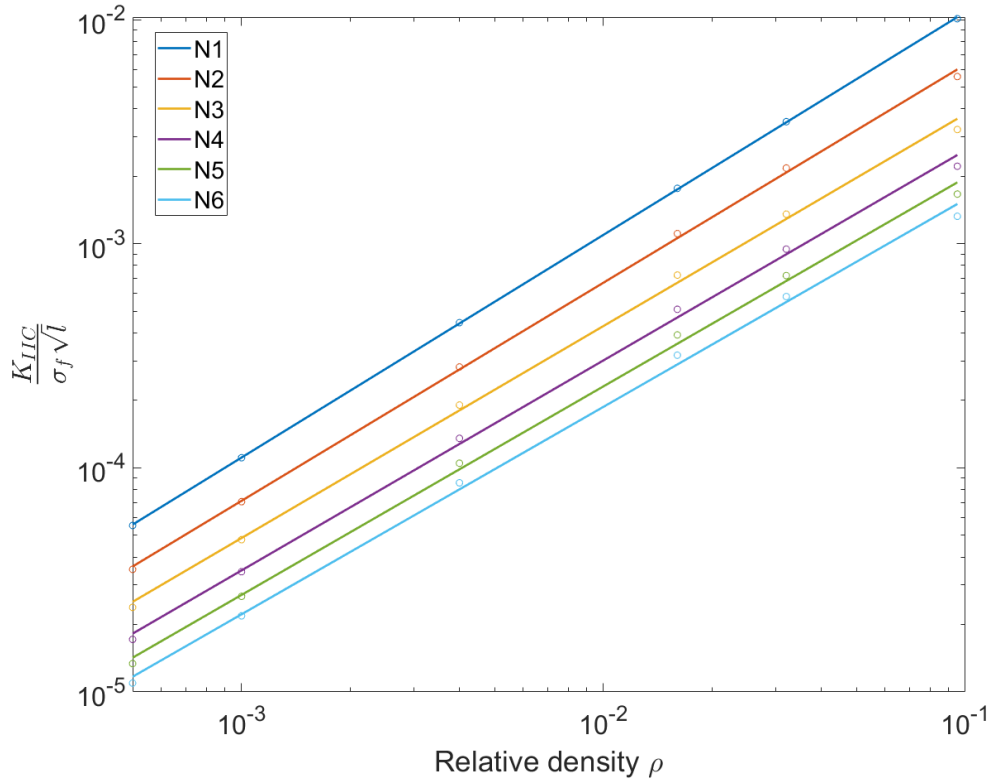


Figure 36: Mode II fracture toughness as a function of relative density.

Table 10: Mode II fracture toughness equations when relative density is varied from 0.005 to 0.095.

N	$\frac{K_{IIc}}{\sigma_f \sqrt{l}}$
1	$0.1065 \bar{\rho}^{0.9938}$
2	$0.05935 \bar{\rho}^{0.9734}$
3	$0.03350 \bar{\rho}^{0.9461}$
4	$0.02262 \bar{\rho}^{0.9373}$
5	$0.01684 \bar{\rho}^{0.9308}$
6	$0.01332 \bar{\rho}^{0.9258}$

Similarly to mode I, the exponent d is approximately unity for $N = 1$ and decreases as N is increased. The maximum stockiness is again limited to 0.002 to assess the effect of stockiness on fracture toughness. The equations for fracture toughness are shown in Table 11 and the exponent d is approximately unity when stockiness is limited to 0.002.

Table 11: Mode II fracture toughness equations when stockiness is limited to a maximum of 0.02.

N	$\frac{K_{IIc}}{\sigma_f \sqrt{l}}$
1	$0.1065 \bar{\rho}^{0.9938}$
2	$0.06687 \bar{\rho}^{0.9923}$
3	$0.04000 \bar{\rho}^{0.9743}$
4	$0.02955 \bar{\rho}^{0.9788}$
5	$0.02236 \bar{\rho}^{0.9749}$
6	$0.01802 \bar{\rho}^{0.9727}$

4.2.5 Mode II fracture locations

Figure 37 shows a $N = 6$ lattice where relative density is 0.095 under mode II loading. A horizontal shear band can be seen ahead of the crack tip. The deformed shape is similar for all the values of N .

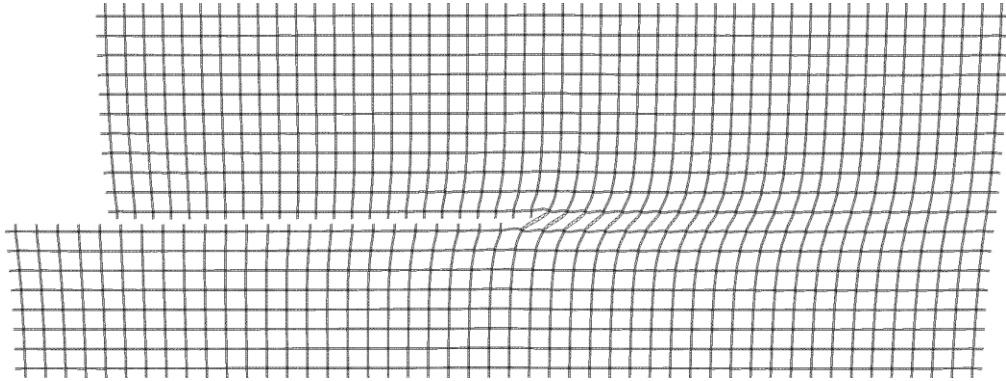


Figure 37: Deformed lattice under mode II loading when $N = 6$ and $\bar{\rho} = 0.095$.

The first strut to fail is presented in Figure 38 for a lattice where $N = 3$ for simplicity. The strut marked in green is the first strut to fail when $N = 1$. The struts marked with blue are the struts that fail when $N = 2$ or $N = 3$ and the relative density is low. The struts marked in red are the struts that fail for $N = 2$ and $N = 3$ at high relative density and values of N higher than 3. This indicates that stockiness dictates the failure location. At low stockiness one of the blue struts fails and at high stockiness one of the red struts fails. Examining the beam elements revealed that bending induced axial stress is higher on the red struts compared to the blue struts. This is likely the reason for the failure location change as bending induced axial stress increases with beam thickness.

The location of the first failure also dictates the direction of crack propagation. If the strut that fails is located in the blue area then the crack

propagates downwards. Otherwise, if fracture occurs in the red area the crack propagates to the right.

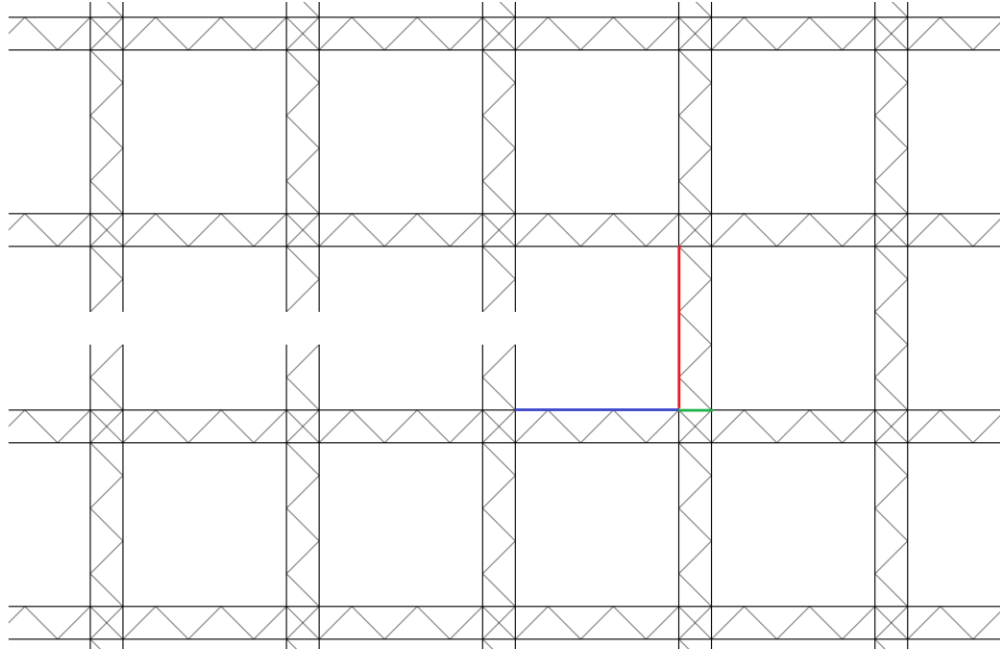


Figure 38: Mode II failure location.

The fracture pattern for $N = 1$ is shown in Figure 39. The fracture toughness increases after the first strut A is broken when relative density is less than 0.032. For higher relative density the maximum fracture toughness occurs when strut A is broken. Examining the beam elements at struts A and B reveals that strut B experiences more bending compared to strut A . The increase in fracture toughness is approximately 10% at relative density of 0.032 or lower.

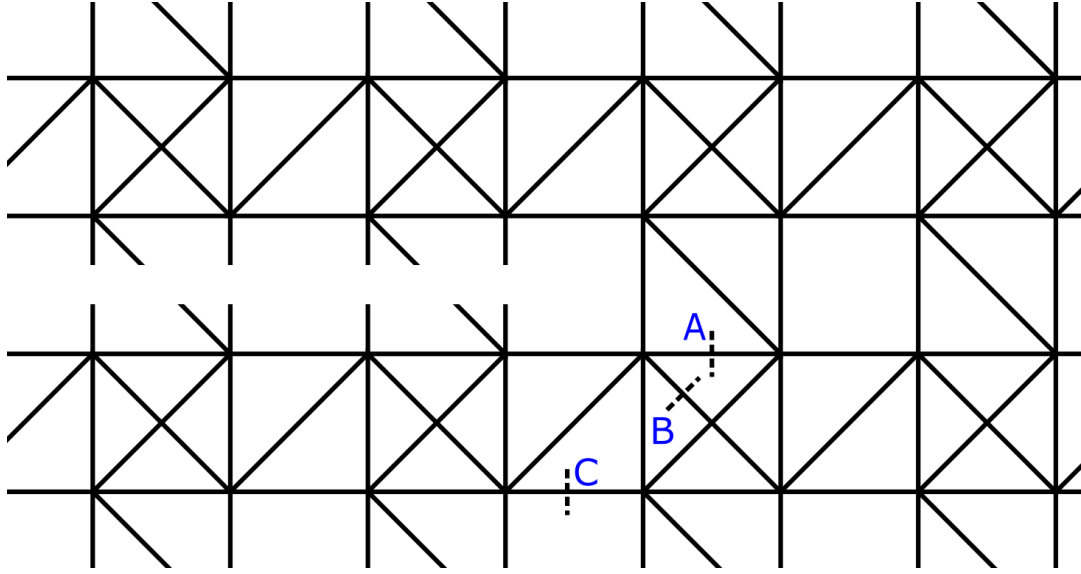


Figure 39: Mode II fracture pattern for $N = 1$ lattice.

The fracture pattern of a $N = 3$ lattice at a relative density of 0.004 or lower is shown in Figure 40. The fracture pattern is similar to $N = 2$ at relative density of 0.032 or lower. An increase in fracture toughness is observed corresponding to strut C breaking, but this is not considered in the results due to possible changes in the boundary displacement field caused by struts A and B breaking.

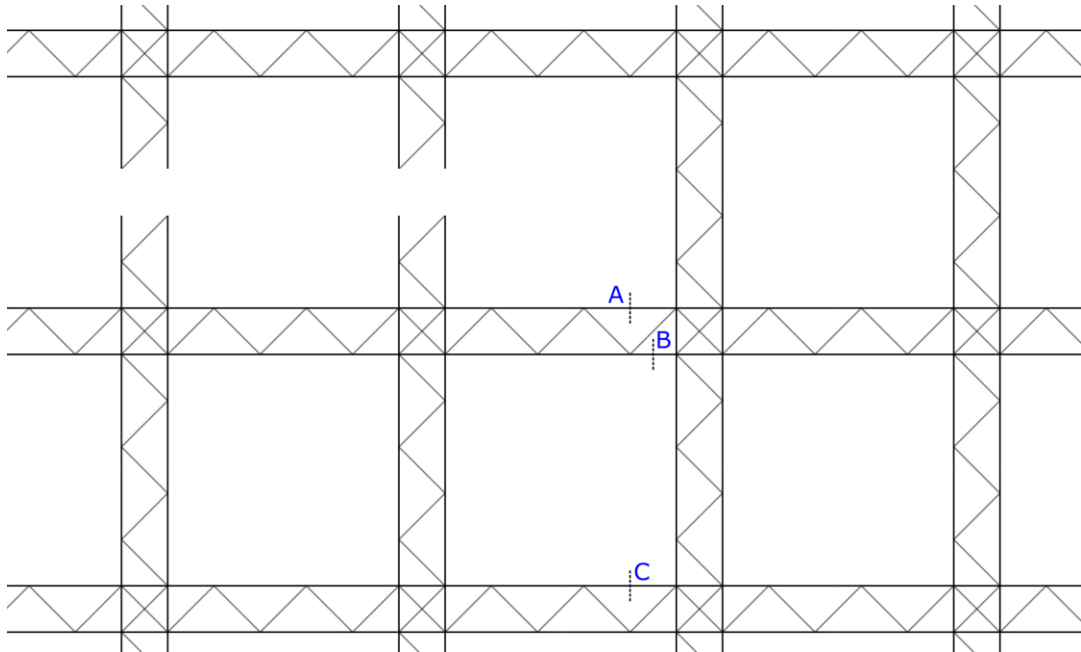


Figure 40: Mode II fracture pattern for $N = 3$ lattice at low relative density.

The fracture pattern of $N = 3$ at high relative density is given in Figure 41. The fracture pattern is similar to $N = 2$ at high relative density and higher

values of N . The fracture pattern is also similar to the mode I fracture pattern. It is observed that fracture toughness corresponding to strut C breaking is higher than strut A , but this is not considered in the results due to reason outlined in section 4.2.3.

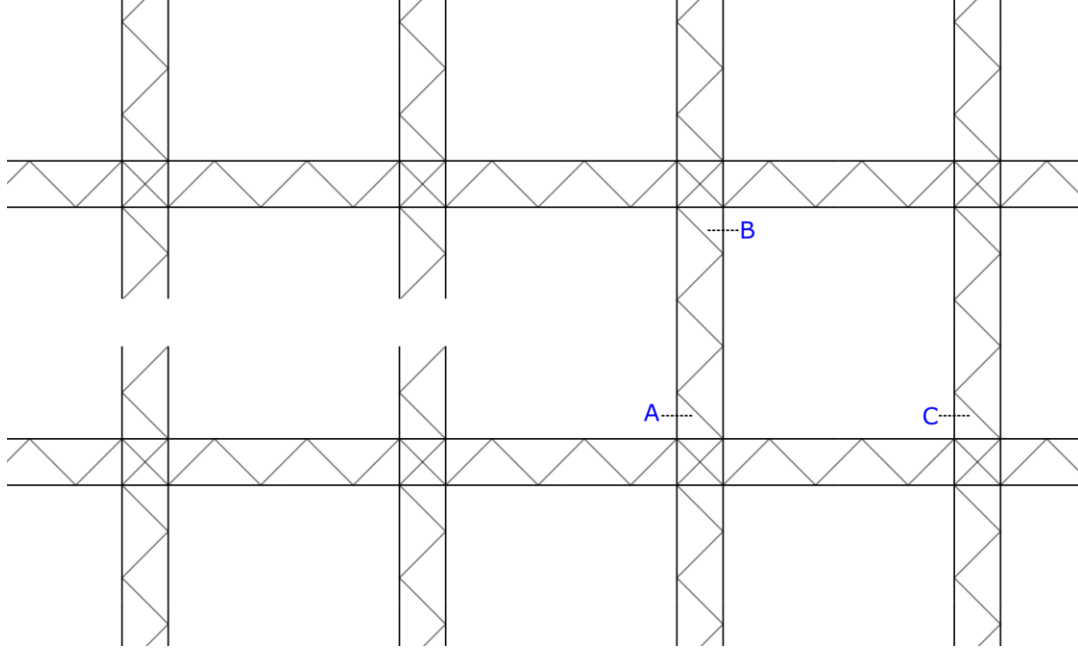


Figure 41: Mode II fracture pattern for $N = 3$ lattice at high relative density.

4.3 Comparison to nonhierarchical square

The mode I fracture toughness of a hierarchical square is comparable to that of a nonhierarchical square lattice as shown in Figure 42. The fracture toughness for a nonhierarchical square was obtained by Romijn and Fleck (2007), who also obtained the fracture toughness using a boundary layer analysis. Hierarchical square where $N = 1$ manages slightly higher mode I fracture toughness due to the fracture toughness increasing after the initial strut failure as detailed in section 4.2.3. Higher values of N result in a slightly lower fracture toughness compared to the nonhierarchical square as relative density increases.

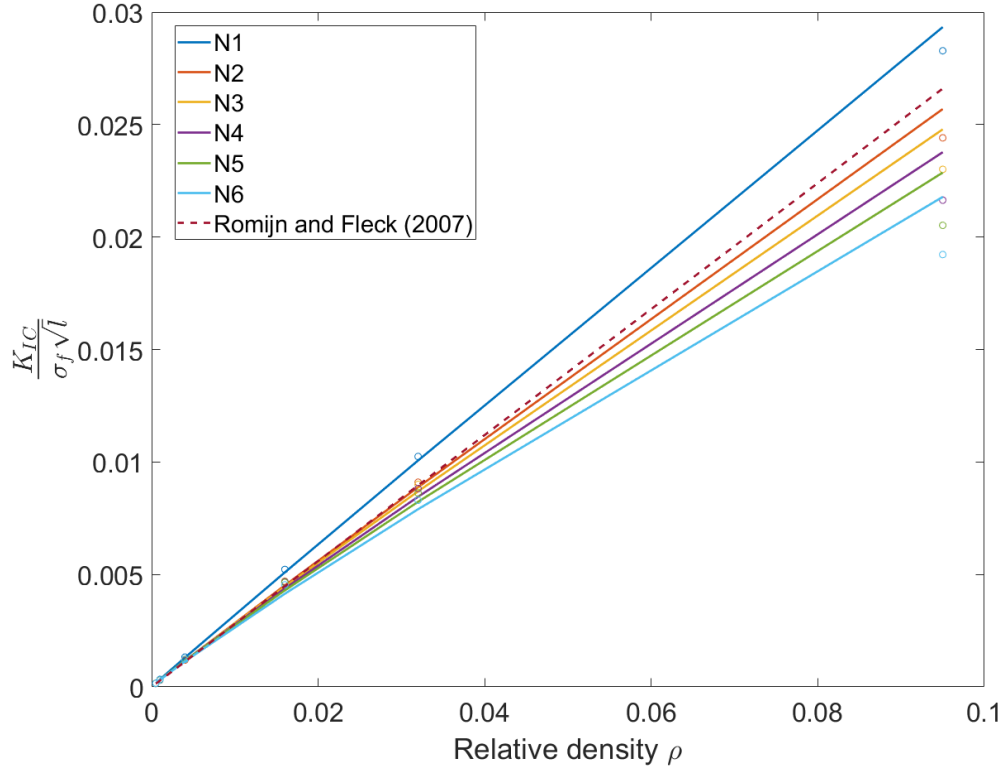


Figure 42: Mode I fracture toughness compared to nonhierarchical square.

The mode II fracture toughness of the hierarchical square is considerably higher than the fracture toughness of the nonhierarchical square, especially at low relative densities, see Figure 43. This is due to the power-law exponent d , which is 1.5 for the nonhierarchical square while for the hierarchical square it is equal to unity. The fracture toughness of nonhierarchical square exceeds the fracture toughness of the hierarchical square only at high relative density. The fracture toughness of $N = 1$ hierarchical square is not exceeded at all in the feasible relative density range.

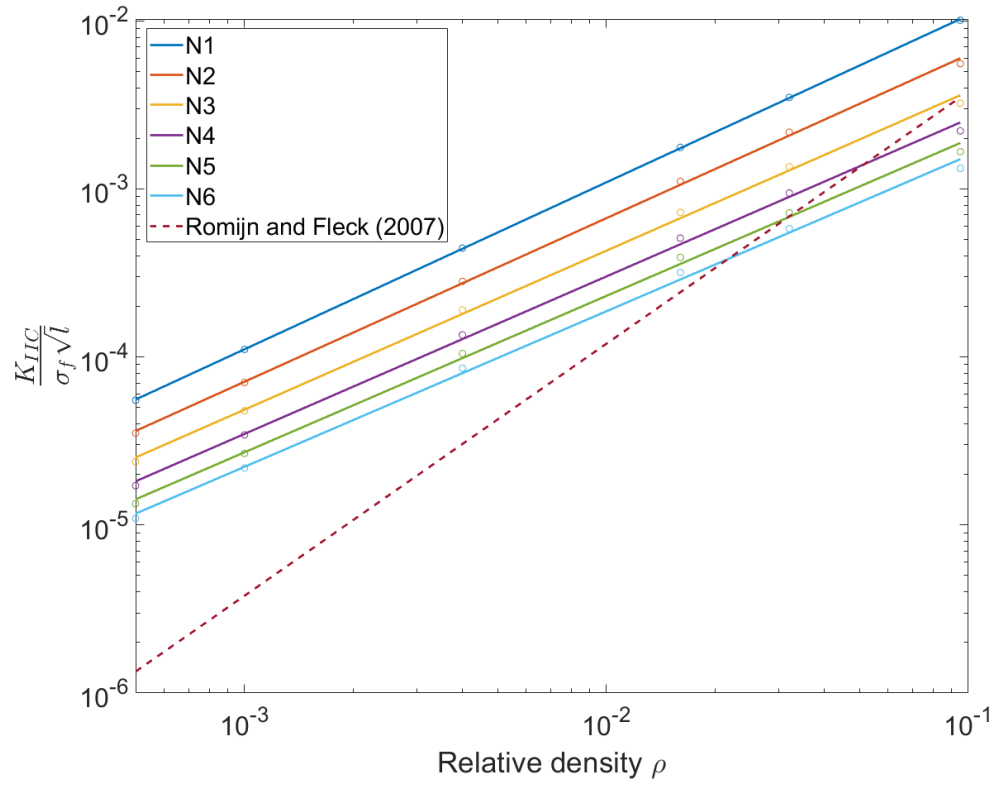


Figure 43: Mode II fracture toughness compared to nonhierarchical square.

5 Conclusions and outlook

The hierarchical square lattice where $N = 1$ is the best performing topology in terms of in-plane elastic properties and fracture toughness. This is due to the shear modulus and mode II fracture toughness greatly decreasing when the value of N is increased making hierarchical squares with high values of N less desirable. The shear modulus and mode II fracture toughness are also the material properties where the $N = 1$ topology outperforms the nonhierarchical square. This is due to the hierarchical square unit cell containing more struts which form a stretching-dominated lattice material instead of a bending-dominated material. For hierarchical square, the exponent of the power-law for the shear modulus is unity while for a simple square, it is 3. This means that the hierarchical square has a much higher shear modulus. The mode II fracture toughness power-law exponent for the hierarchical square is unity, whereas it is 1.5 for a simple, and this results in a much higher fracture toughness for the hierarchical square.

Compared to other stretching-dominated lattice materials the Young's modulus of the hierarchical square is similar although slightly less than the nonhierarchical square due to the inclined struts which carry negligible load. The shear modulus of the hierarchical square is lower than other stretching-dominated lattice materials. The mode I fracture toughness of the hierarchical square is comparable to other stretching-dominated lattices, but the mode II fracture toughness is lower.

The scope of this master's thesis was limited to only examining the response of a perfect lattice. In reality the cell wall tensile strength is not constant, and lattices can contain missing struts or misplaced joints. Further study of the hierarchical square lattice could examine the effect of such imperfections on the in-plane elastic properties and fracture toughness.

The main advantage of introducing hierarchy to the square topology was the transition from a bending-dominated response under shear loading to a stretching-dominated response. In the future, introducing hierarchy to already stretching-dominated lattices could be examined.

6 References

- Abaqus documentation. Available at: <https://abaqus-docs.mit.edu/2017/English/SIMACAEEXCRefMap/simaexc-c-docproc.htm#simaexc-c-docproc-t-UsingADocumentation-sma-topic1> (Accessed: 28 March 2022)
- Ashby, M. (2011) 'Hybrid Materials to Expand the Boundaries of Material-Property Space', *Journal of the American Ceramic Society*, 94, pp. 3-14. doi: <https://doi-org.libproxy.aalto.fi/10.1111/j.1551-2916.2011.04559.x>
- Calladine, C. R. (1978) 'Foam topology: bending versus stretching dominated architectures', *International Journal of Solids and Structures*, 14(2), pp. 161-172. doi: [https://doi.org/10.1016/0020-7683\(78\)90052-5](https://doi.org/10.1016/0020-7683(78)90052-5)
- Deshpande, V. S., Ashby, M. F. and Fleck, N. A. (2000) 'Foam Topology Bending Versus Stretching Dominated Architectures', *Acta Materialia*, 49(6), pp. 1035-1040. doi: [https://doi.org/10.1016/S1359-6454\(00\)00379-7](https://doi.org/10.1016/S1359-6454(00)00379-7)
- Fan, H. L., Jin, F. N., Fang, D. N. (2008) 'Mechanical properties of hierarchical cellular materials. Part I: Analysis' *Composites Science and Technology*, 68(15-16), pp. 3380-3387. doi: <https://doi.org/10.1016/j.comp-scitech.2008.09.022>
- Fleck, N. A., Qiu, X. (2007) 'The damage tolerance of elastic–brittle, two-dimensional isotropic lattices', *Journal of the Mechanics and Physics of Solids*, 55(3), pp. 562-588. doi: <https://doi.org/10.1016/j.jmps.2006.08.004>
- Fleck, N. A., Deshpande, V. S., Ashby, M. F. (2010) 'Micro-architected materials: past, present and future', *Proceedings of the Royal Society*, 466(2121), pp. 2495-2516. doi: <https://doi.org/10.1098/rspa.2010.0215>
- Gu, H., Pavier, M., Shterenlikht, A. 'Experimental study of modulus, strength and toughness of 2D triangular lattices', *International Journal of Solids and Structures*, 152-153, pp. 207-216. doi: <https://doi.org/10.1016/j.ijsol-str.2018.06.028>
- Hsieh, M., Deshpande, V. S., Valdevit, L. (2020) 'A versatile numerical approach for calculating the fracture toughness and R-curves of cellular materials', *Journal of the Mechanics and Physics of Solids*, 138, doi: <https://doi.org/10.1016/j.jmps.2020.103925>

Huang, J. S., Gibson, L. J. (1991) 'Fracture toughness of brittle foams', *Acta Metallurgica et Materialia*, 39(7), pp. 1627-1636. doi: [https://doi.org/10.1016/0956-7151\(91\)90250-5](https://doi.org/10.1016/0956-7151(91)90250-5)

Irwin, G. R. (1957) 'Analysis of Stresses and Strains Near the End of a Crack Traversing a Plate', *Journal of Applied Mechanics*, 24(3), pp. 361-364. doi: <https://doi-org.libproxy.aalto.fi/10.1115/1.4011547>

Kooistra, G. W., Deshpande, V., Wadley, N. G. (2007) 'Hierarchical Corrugated Core Sandwich Panel Concepts', *Journal of Applied Mechanics*, 74(2), pp. 259-268. doi: <https://doi-org.libproxy.aalto.fi/10.1115/1.2198243>

Launey, M. E., Ritchie, R. O. (2009) 'On the Fracture Toughness of Advanced Materials', *Advanced Materials*, 21(20), pp. 2103-2110. doi: <https://doi-org.libproxy.aalto.fi/10.1002/adma.200803322>

Lipperman, F., Ryvkin, M., Fuchs, M. B. (2007) 'Fracture toughness of two-dimensional cellular material with periodic microstructure', *International Journal of Fracture*, 146(4), pp. 279-290. doi: <https://doi-org.libproxy.aalto.fi/10.1007/s10704-007-9171-5>

Lynch, S. P., Wanhill, R. J. H., Byrnes, R. T., Bray, G. H. (2014) 'Fracture Toughness and Fracture Modes of Aerospace Aluminum-Lithium Alloys', *Aluminum-Lithium Alloys*, pp. 415-455. doi: <https://doi.org/10.1016/B978-0-12-401698-9.00013-6>

Maiti, S.K., Ashby, M.F., Gibson, L.J. (1984) 'Fracture toughness of brittle cellular solids', *Scripta Metallurgica*, 18(3), pp. 213-217. doi: [https://doi.org/10.1016/0036-9748\(84\)90510-6](https://doi.org/10.1016/0036-9748(84)90510-6)

Maxwell J. C. (1864) 'L. On the calculation of the equilibrium and stiffness of frames', *Philosophical Magazine*, 24(182), pp. 294-299. doi: <https://doi.org/10.1080/14786446408643668>

Romijn, N. E., Fleck, N. A. (2007) 'The fracture toughness of planar lattices: imperfection sensitivity', *Journal of the Mechanics and Physics of Solids*, 55(12), pp. 2538-2564. doi: <https://doi.org/10.1016/j.jmps.2007.04.010>

Schmidt, I., Fleck, N. A. (2001) 'Ductile fracture of two-dimensional cellular structures', *International Journal of Fracture*, 111(4), pp. 327-342. doi: <https://doi-org.libproxy.aalto.fi/10.1023/A:1012248030212>

Sih, G. C., Paris, P. C., Irwin, G. R. (1965) 'On cracks in rectilinearly anisotropic bodies', *International Journal of Fracture*, 1, pp. 189–203. doi: <https://doi-org.libproxy.aalto.fi/10.1007/BF00186854>

Tankasala, H. C., Deshpande, V. S., Fleck, N. A. (2017) 'Tensile response of elastoplastic lattices at finite strain', *Journal of the Mechanics and Physics of Solids*, 109, pp. 307-330. doi: <https://doi.org/10.1016/j.jmps.2017.02.002>

Tsang, H. H. et al. (2019), 'Energy absorption of muscle-inspired hierarchical structure: Experimental investigation', *Composite Structure*, 226. doi: <https://doi.org/10.1016/j.compstruct.2019.111250>

Wang, A., McDowell, D. L. (2004) 'In-Plane Stiffness and Yield Strength of Periodic Metal Honeycombs', *Journal of Engineering Materials and Technology*, 126(2), pp. 137–156. doi: <https://doi-org.libproxy.aalto.fi/10.1115/1.1646165>

Williams, M., L. (1957) 'On the Stress Distribution at the Base of a Stationary Crack', *Journal of Applied Mechanics*, 24(1), pp. 109-114. doi: <https://doi-org.libproxy.aalto.fi/10.1115/1.4011454>

Wu, W., Owino, J., Al-Ostaz, A., Cai, L. (2014) 'Applying Periodic Boundary Conditions in Finite Element Analysis', 2014 SIMULIA Community Conference, pp. 707-719. Available at: <https://imechanica.org/files/pbc.pdf> (Accessed: 28 February 2022)